



**João Nuno Santos
Gonçalves**

**Cálculos de estrutura electrónica e parâmetros
hiperfinos em óxidos**



**João Nuno Santos
Gonçalves**

**Calculations of electronic structure and hyperfine
parameters in oxides**

Dissertação apresentada à Universidade de Aveiro para cumprimento dos requisitos necessários à obtenção do grau de Mestre em Engenharia Física, realizada sob a orientação científica do Prof. Doutor Vítor Amaral, Professor Associado com agregação, do Departamento de Física da Universidade de Aveiro.

Apoio financeiro da FCT no âmbito dos
projectos POCI/FP/63438/2005 e
POCI/FP/63953/2007.

acknowledgments

I would like to thank my supervisor for accepting me as a student and for supervising my work during the thesis. My special thanks for giving me the opportunity to work in a great environment with all the facilities at my disposal.

On that note I also would like to thank Dr. João Guilherme Correia for providing me with computers specifically configured to use during my thesis, and for his help on various physics topics. While I was at CERN I must thank the group with whom I worked as a whole, their help was essential to understand most of the things. In particular João Amaral and Armandina Lopes also gave me valuable hints the rest of the time when I was at Aveiro.

Special thanks to Dr. Heinz Haas, who gave me a first course and taught me the basic things about the computational method, and continued to answer my questions throughout the year.

This work was supported by grants from the projects POCI/FP/63438/2005 and POCI/FP/63953/2007.

palavras-chave

Óxidos magnéticos, manganites, propriedades hiperfinas, método computacional, ab initio, perturbações de correlação angular

resumo

Cálculos de primeiros princípios de estrutura electrónica são efectuados em óxidos de manganês LaMnO_3 e CaMnO_3 para obter gradientes de campo eléctrico hiperfinos. Os resultados dos cálculos são comparados com resultados experimentais e de outros cálculos de primeiros princípios. Uma descrição das interações hiperfinas é seguida de uma introdução ao gradiente de campo eléctrico e ao método de espectroscopia de perturbações de correlação angular, descrevendo detalhes experimentais. De seguida uma descrição geral de manganites de terras raras com estrutura do tipo perovskite é apresentada, com ênfase em LaMnO_3 e aspectos estruturais. A base teórica do método computacional aplicado nestes materiais é também apresentada para melhor compreensão dos resultados obtidos. Dos resultados e da discussão concluímos que é possível obter valores de campo eléctrico com uma precisão aceitável quando comparado com os cálculos de primeiros princípios para o LaMnO_3 , e para o CaMnO_3 é certamente possível melhorar os resultados. Os resultados obtidos seguem a variação esperada para o CaMnO_3 , pelo menos qualitativamente.

keywords

Magnetic oxides, manganites, hyperfine properties, computational method, ab initio, perturbed angular correlation

abstract

First principles calculations of electronic structure are done on perovskite manganese based oxides LaMnO_3 and CaMnO_3 to obtain the hyperfine electric field gradients. The calculated results are compared with experimental and other first-principles results. A description of hyperfine interactions is followed by an introduction to the electric field gradient and the perturbed angular correlation spectroscopy, explaining experimental details of this method. Next, a general description of rare earth perovskite type manganites, is presented, with emphasis on LaMnO_3 and structural aspects. The theoretical basis of the computational method applied on these materials is also presented for better understanding of the results obtained. These results finish with a discussion and a conclusion. From the results and discussion we conclude that the values of the electric field gradient can be calculated with acceptable precision when compared with other first principles results on LaMnO_3 , and for CaMnO_3 it is certainly possible to improve the results. The qualitative results obtained for CaMnO_3 , however, follow the expected variation.

Electronic structure calculations and
determination of hyperfine parameters in
manganese oxides

João Nuno Santos Gonçalves

July 19, 2007

Contents

1	Hyperfine interactions	5
1.1	Hyperfine interactions	5
1.1.1	Electric Interaction	5
1.1.2	Magnetic Interaction	10
1.2	Perturbed Angular Correlations	11
1.2.1	PAC sources and experimental details	12
1.2.2	Theory and analysis of spectra	15
2	Perovskite type manganese based oxides	20
2.1	Structure	20
2.1.1	Ideal Perovskite Structure	20
2.1.2	Crystal structure	21
2.1.3	Colossal magnetoresistance	23
2.1.4	Double exchange and super exchange	24
2.1.5	Other properties	25
3	Concepts of electronic structure calculations	29
3.1	Density functional theory	29
3.1.1	Wave Function	29
3.1.2	Hohenberg-Kohn theorems	31
3.1.3	Thomas-Fermi model	32
3.1.4	Kohn-Sham method	32
3.1.5	Approximations	33
3.1.6	Basis sets	36
3.2	Electric field gradient in LAPW	41
4	Results and discussion	42
4.1	Method	42
4.2	CaMnO ₃	43
4.3	LaMnO ₃	45
4.3.1	Previous work	45

4.3.2 Results	46
5 Conclusion	50

Introduction

Since the recent discovery of colossal magnetoresistance on thin films of rare-earth manganese based perovskite-type oxides[1], known as manganites, these compounds have been the subject of extensive research. These oxides are of the form $R_{1-x}A_xMnO_3$, with A a divalent alkaline earth and R a trivalent rare-earth cation. Compounds such as $La^{3+}Mn^{3+}O_3^{2-}$ and $Ca^{2+}Mn^{4+}O_3^{2-}$, can easily be grouped to form mixed-valence compounds (in this example $La_xCa_{1-x}MnO_3$), which exhibit many interesting properties that can be observed by varying their composition with x . After more than a decade of increasing research the basic mechanisms that drive the change of their properties are not yet fully understood.

A few years after the discovery of these compounds[2, 3, 4], the properties of the first manganites studied were apparently explained by the formulation of the double exchange interaction [5, 6]. But today it is understood that double exchange is not enough to explain all the states of these materials (which include ferromagnetic metal and insulator, charge/orbital order and others). It is now believed that other aspects such as electron-phonon coupling, phase separation, magnetic, charge and orbital order play a major role.

With the rapid growth of computational power and discovery of computationally friendly theories, it is now possible to do simulations on complex materials. Since these oxides appear to be quite difficult to describe in purely analytical frameworks, these type of calculations is very useful and needed to reach further understanding.

In this work Wien2k[7], a computational tool based on density functional theory(ch. 3.1) was applied, making first-principle calculations on these compounds. Hypothetical idealized structures and experimentally obtained data were used to obtain the output of electronic structure calculations. From the data obtained, the electric field (EFG) gradient was analyzed in more detail.

Nuclear hyperfine techniques, that measure the hyperfine quantities like EFG and magnetic hyperfine field, are useful to provide local atomic scale information on the charge distribution or local spin density transfer, due

to the interaction between the probe isotope and the lattice host. I used the simulations with the main objective of calculating the EFG on specific sites of manganites. To determine the electric field gradient, the contributions of neighboring ionic cores, electrons of the probe core and conduction electrons must be calculated. The calculation of the spatial distribution of conduction electrons is particularly difficult and requires extremely accurate band-structure calculations. Further understanding of these quantities in manganites is extremely useful since they provide local information and this is crucial for these materials which have intrinsic inhomogeneities at the near atomic scale.

This work starts with a description of hyperfine interactions in the first chapter, and a brief exposition of a technique used to measure those quantities, perturbed angular correlations (PAC). The work at ISOLDE-CERN, where radioactive probes can be produced and samples can be studied with PAC is described. This is a particularly useful method to measure hyperfine interactions, because it has the added advantage (in comparison with other nuclear techniques such as NQR and NMR), of allowing measurements in a wider range of temperatures, with adequate probe elements. Chapter two deals with the basic properties of manganites, especially the ones used for the calculations such as the crystalline structure, and discuss previous work on these materials. In the next chapter the theory in which the computational method is based is also described. The results of simulations, with the details used for the calculations and discussion of results constitute the fourth chapter.

Chapter 1

Hyperfine interactions

1.1 Hyperfine interactions

A nucleus interacts with the electromagnetic field due to the surrounding electronic and nuclear density. In a solid, such fields are produced by the electrons and nuclei in the vicinity of the interacting nucleus, or there may be external fields applied. This is called a hyperfine interaction. The precise measurement of this interaction determines in a very accurate way the internal fields in a solid. This chapter deals with hyperfine interactions and the particular method of perturbed angular correlation spectroscopy. A more detailed exposition of hyperfine interactions can be found in [8].

1.1.1 Electric Interaction

In a given atom or group of atoms, the electric potential $\Phi(\mathbf{r})$ interacts with a nuclear charge distribution $\rho(\mathbf{r})$. This interaction is given by an energy, described classically as

$$E = \int \rho(\mathbf{r})\Phi(\mathbf{r})d^3r. \quad (1.1)$$

With a multipole expansion of the electric potential in a Taylor series around $\mathbf{r} = 0$,

$$\Phi(\mathbf{r}) = \Phi_0 + \sum_{\alpha=1}^3 \left(\frac{\partial\Phi}{\partial x_\alpha} \right)_0 + \frac{1}{2} \sum_{\alpha,\beta} \left(\frac{\partial^2\Phi}{\partial x_\alpha \partial x_\beta} \right)_0 x_\alpha x_\beta + \dots \quad (1.2)$$

the energy can also be expanded:

$$E = E^{(0)} + E^{(1)} + E^{(2)} + \dots, \quad (1.3)$$

where

$$E^{(0)} = \Phi_0 \int \rho(\mathbf{r}) d^3r \quad (1.4)$$

$$E^{(1)} = \sum_{\alpha=1}^3 \left(\frac{\partial \Phi}{\partial x_\alpha} \right)_0 \int \rho(\mathbf{r}) x_\alpha d^3r \quad (1.5)$$

$$E^{(2)} = \frac{1}{2} \sum_{\alpha,\beta} \left(\frac{\partial^2 \Phi}{\partial x_\alpha \partial x_\beta} \right)_0 \int \rho(\mathbf{r}) x_\alpha x_\beta d^3r \quad (1.6)$$

$E^{(0)}$ is the Coulomb energy of a point-like charge distribution in the external potential. It can be written $E^{(0)} = \Phi_0 Z e$, so it is the same for all isotopes of a given element. The second term represents an electric dipole interaction between the electric field ($E = \nabla \Phi$) at the origin and the electric dipole moment of the nuclear charge distribution. Since the nuclear states have definite parity, $\int \rho(\mathbf{r}) x_\alpha d^3r = E^{(1)} = 0$. As for the third term, $E^{(2)}$, it can be separated in two terms:

$$E^{(2)} = E_C + E_Q, \quad (1.7)$$

where

$$E_C = \frac{e}{6\epsilon_0} |\psi(0)| \int \rho(r) d^3r \quad (1.8)$$

$$E_Q = \frac{1}{2} \sum_{\alpha} \Phi_{\alpha\alpha} \int \rho(\mathbf{r}) \left(x_\alpha^2 - \frac{r^2}{3} \right) d^3r \quad (1.9)$$

are called the monopole term and the electric quadrupole interaction respectively.¹

¹These two terms can be derived diagonalizing the matrix $\Phi_{\alpha\beta}$ defined as

$$\Phi_{\alpha\beta} = \left(\frac{\partial^2 \Phi}{\partial x_\alpha \partial x_\beta} \right).$$

After diagonalization,

$$E^{(2)} = \frac{1}{2} \sum_{\alpha} \Phi_{\alpha\alpha} \int \rho(\mathbf{r}) x_\alpha^2 d^3r = \frac{1}{6} \sum_{\alpha} \Phi_{\alpha\alpha} \int \rho(\mathbf{r}) r^2 d^3r + \frac{1}{2} \sum_{\alpha} \Phi_{\alpha\alpha} \int \rho(\mathbf{r}) \left(x_\alpha^2 - \frac{r^2}{3} \right) d^3r$$

with the variable $r^2 = x_1^2 + x_2^2 + x_3^2$. Using also the Poisson equation,

$$(\nabla^2 \Phi)_0 = \sum_{\alpha} \Phi_{\alpha\alpha} = \frac{e}{\epsilon_0} |\psi(0)|^2,$$

the separation in the two terms 1.8 and 1.9 can be obtained.

The Monopole Term E_C

The monopole term E_C depends only on the mean square nuclear radius

$$\langle r^2 \rangle = \frac{1}{Ze} \int \rho(\mathbf{r}) r^2 d^3r \quad (1.10)$$

E_C gives a shift of the nuclear levels, describing the electrostatic interaction of an *extended* nuclear charge distribution $\rho(\mathbf{r})$ with the electrons at the nuclear site.

The monopole term can be written

$$E_C = \frac{Ze^2}{6\epsilon_0} |\psi(0)|^2 \langle r^2 \rangle \quad (1.11)$$

This term is responsible for the isotope shift. It causes spectral lines of two isotopes with different nuclear radii to be slightly different.

The Electric Quadrupole Interaction E_Q

E_Q contains the integral $\int \rho(\mathbf{r})(x_\alpha^2 - r^2/3)d^3r$. For $x_\alpha = z$, this integral is $(e/3)$ times the classical quadrupole moment of the nucleus. Substituting in 1.9 we can write

$$E_Q = \frac{e}{6} \sum_{\alpha} \Phi_{\alpha\alpha} Q_{\alpha\alpha} \quad (1.12)$$

where the quadrupole tensor moment is

$$Q_{\alpha\alpha} = \frac{1}{e} \int \rho(\mathbf{r})(3x_\alpha^2 - r^2)d^3r$$

The terms $\Phi_{\alpha\alpha}$ contribute to the trace ($\nabla^2\Phi = \sum \Phi_{\alpha\alpha}$). Defining $V_{\alpha\alpha}$

$$\Phi_{\alpha\alpha} = V_{\alpha\alpha} + \frac{1}{3}(\nabla^2\Phi), \quad (1.13)$$

one can see that the matrix $V_{\alpha\alpha}$ is traceless. $V_{\alpha\alpha}$ is called the electric field gradient(EFG). Substituting Eq. 1.13 in Eq. 1.12, the portion $(1/3)(\nabla^2\Phi)$ does not contribute to E_Q since $\sum Q_{\alpha\alpha}$ is zero. Then E_Q simply results in these quantities as

$$E_Q = \frac{e}{6} \sum_{\alpha} V_{\alpha\alpha} Q_{\alpha\alpha}. \quad (1.14)$$

Electric Field Gradient

The electric field gradient $V_{\alpha\alpha}$ is a symmetric traceless tensor of rank two. Because it is a symmetric traceless tensor, the electric field gradient is completely described by five parameters, with a 3x3 symmetric traceless matrix. In spherical coordinates, it can be represented by five 'angular momentum' components of rank two ($L=2$, $M=-2,-1,0,1,2$). By appropriate choice of the principal axis system, one can choose $|V_{zz}| \geq |V_{yy}| \geq |V_{xx}|$. The principal component is V_{zz} (or $V_{20} = \frac{1}{4}\sqrt{\frac{5}{\pi}}V_{zz}$) in spherical coordinates). Generally, one chooses to describe the electric field gradient by V_{zz} and the asymmetry parameter η ,

$$\eta = \frac{V_{xx} - V_{yy}}{V_{zz}}. \quad (1.15)$$

The electric field gradient tensor is also defined as the second derivative of the electric potential with respect to spacial coordinates, at the nuclear position:

$$V_{ij} = \frac{\partial^2 V(0)}{\partial x_i \partial x_j} \quad (1.16)$$

$V_{\alpha\alpha}$ are the principal values. Only charges not at the nuclear site contribute to $V_{\alpha\alpha}$.

For spherically symmetric charge distributions (s electrons), $V_{xx} = V_{yy} = V_{zz}$. Since $\sum V_{\alpha\alpha} = 0$, all components of the electric field gradient are zero and cannot contribute to the energy E_Q .

The electric quadrupole interaction E_Q is a product of the nuclear electric quadrupole moment and the electric field gradient at the nuclear position (eq. 1.14, the nuclear quadrupole interaction). The representation of the nuclear quadrupole moment and the electric field gradient by spherical tensors in the quantum formulation[9] allows us to write the nuclear electric quadrupole tensor in terms of the $3j$ symbols and $L = 2$ spherical harmonics of the nuclear angular momentum I .

$$Q_{2q} = Zr^2 Y_2^q \begin{pmatrix} I & 2 & I \\ -M & 0 & M \end{pmatrix} \langle I || Q_2 || I \rangle$$

For the electric field gradient the tensor components are

$$V_{20} = \frac{1}{4}\sqrt{\frac{5}{\pi}}V_{zz}$$

$$V_{2\pm 1} = \pm \frac{1}{2}\sqrt{\frac{5}{6\pi}}(V_{xz} \pm V_{yz}) \quad (1.17)$$

$$V_{2\pm 2} = \frac{1}{4}\sqrt{\frac{5}{6\pi}}(V_{xx} - V_{yy} \pm 2iV_{xy}) \quad (1.18)$$

In the principal axis system,

$$V_{20} = \frac{1}{4} \sqrt{\frac{5}{\pi}} V_{zz} \quad (1.19)$$

$$V_{2\pm 1} = 0 \quad (1.20)$$

$$V_{2\pm 2} = \frac{1}{4} \sqrt{\frac{5}{6\pi}} (V_{xx} - V_{yy}) = \frac{1}{4} \sqrt{\frac{5}{6\pi}} \eta V_{zz} \quad (1.21)$$

Limiting ourselves to axially symmetric electric field gradients $V_{xx} = V_{yy}$, or $\eta = 0$, calculation of E_Q gives simply

$$E_Q = \frac{3M^2 - I(I+1)}{4I(2I-1)} eQV_{zz}$$

The transition energy between two sublevels M and M' is

$$E_Q(M) - E_Q(M') = \frac{3eQV_{zz}}{4I(2I-1)} |M^2 - M'^2| = 3|M^2 - M'^2| \hbar\omega_Q \quad (1.22)$$

where we have introduced the quadrupole frequency

$$\omega_Q = \frac{eQV_{zz}}{4I(2I-1)\hbar} \quad (1.23)$$

For a non-axial symmetric quadrupole interaction ($\eta \neq 0$) the quadrupole interaction cannot be diagonalized exactly and numerical methods have to be employed.

Because $(M^2 - M'^2) = (M + M')(M - M')$, the quantity $|M - M'^2|$ is always an integer. Thus all transition frequencies are integer multiples of the lowest transition frequency,

$$\begin{cases} \omega_Q^0 = 6\omega_Q & (\text{for half-integer nuclear spin}) \\ \omega_Q^0 = 3\omega_Q & (\text{for integer nuclear spin}) \end{cases}$$

Generally one uses the derived quantity ν_Q

$$\nu_Q = eQV_{zz}/\hbar \quad (1.24)$$

The electric field gradient is proportional to the deviation from cubic symmetry of the electronic charge density. Since it varies with $1/r^3$ it depends primarily on the local environment ($0 \leq 0.2\text{\AA}$) of the probe nucleus, and is sensitive to the phenomena in the near vicinity of the nucleus (up to $\sim \text{\AA}$). In sites with cubic or higher symmetry the gradient has null value.

One way to calculate the electric field gradient is to use a phenomenological model, in which it is a sum of two parts, one from the neighboring ion cores(lattice) and one from the electrons(el), and two correction factors appear.

$$V_{zz} = (1 - \gamma_{\infty})V_{zz}(lattice) + (1 - R)V_{zz}(el) \quad (1.25)$$

The factor γ_{∞} , called the Sternheimer antishielding factor, accounts for the inner-shell polarization of the probe atom, and the factor R accounts for the amplification of the electronic part of the electric field gradient.

Using a simple point charge model it is possible to estimate the EFG. If the ion cores are assumed to be point charges, the contributions of all lattice atoms are summed, except for the probe:

$$V_{\alpha\beta} = \frac{Ze}{4\pi\epsilon_0} \sum_{i \neq 0} \frac{1}{r_i^5} \begin{pmatrix} 3x_i^2 - r_i^2 & 3x_i y_i & 3x_i z_i \\ 3x_i y_i & 3y_i^2 - r_i^2 & 3y_i z_i \\ 3x_i z_i & 3y_i z_i & 3z_i^2 - r_i^2 \end{pmatrix}, \quad (1.26)$$

where \mathbf{r}_i is the vector from the origin to the point charge i . However, the results offered for less simple cases are most of the times wrong or of limited use. The recent increase of computational power allowed the possibility to use much more sophisticated, ab initio methods, like the one used here, that effectively help to complement experimental work and to understand the theory[10].

1.1.2 Magnetic Interaction

The magnetic nuclear moment μ interacts with the magnetic field \mathbf{B} of the electrons at the position of the nucleus. The interaction energy is

$$E_{magn} = -\mu \cdot \mathbf{B} \quad (1.27)$$

This extra energy lifts the degeneracy of the nuclear M states and induces a precession of the nuclear spin.

Level splitting

Quantization of the angular momentum allows only certain directional possibilities for μ with respect to \mathbf{B} . Choosing the z axis parallel to \mathbf{B} , one obtains

$$\begin{aligned} E_{magn} &= \langle I, M | -\mu_z B_z | I, M \rangle \\ &= -\gamma B_z \langle I, M | I_z | I, M \rangle = \gamma B_z \hbar M \end{aligned} \quad (1.28)$$

The energy difference between adjacent M levels is

$$E_{magn}(M + 1) - E_{magn}(M) = -\gamma\hbar B_z = -g\mu_N B_z \quad (1.29)$$

$\mu_N = \frac{e\hbar}{2m_P} = 5.05 \times 10^{-27} Am^2$, where m_P is the proton mass, is the nuclear magneton. The dimensionless factor g can be calculated from an angular momentum scheme and gives approximate values, or can be obtained experimentally. The gyromagnetic ration of nuclei is $\gamma = g\mu_N/\hbar$. With a few exceptions, this means that the splitting is the same between all neighboring M levels.

Nuclear Spin Precession

The magnetic interaction causes a time dependence in the expectation values of the nuclear properties. The time dependence wave function is

$$\psi(t) = \Lambda(t)\psi(0) \quad (1.30)$$

where $\Lambda(t) = \exp(-iHt/\hbar)$. $H = -\gamma I_z B_z$ is the Hamiltonian operator and $\Lambda(t)$ is the time evolution operator. Substituting one obtains

$$\Lambda(t) = \exp[-i(-\gamma I_z B_z)t/\hbar] = \exp[-i(-\gamma B_z t)I_z/\hbar] \quad (1.31)$$

$\Lambda(t)$ in Eq. (1.31) has the form of a rotation operator around the z axis and can be written

$$\Lambda(t) = \exp(-i\alpha I_z/\hbar) \quad (1.32)$$

where α is the rotation angle. From Eqs. (1.32) and (1.30) one can see that the classical Larmor frequency

$$\omega_L = -\gamma B_z = -g(\mu_N/\hbar)B_z \quad (1.33)$$

appears in the time evolution of the state. The expectation value of the angular momentum \mathbf{I} calculated with wave functions of the form in Eq. 1.30 precess around \mathbf{B} with frequency ω_L .

The magnetic hyperfine fields can be calculated theoretically with first principles calculations, but will not be dealt with in this work.

1.2 Perturbed Angular Correlations

One experimental technique used to obtain the quadrupole frequencies with local probes is the $\gamma - \gamma$ perturbed angular correlation method (PAC). It

measures the time dependence of the γ -ray emission pattern of a probe, a radioactive isotope doped in the material to study. A function that measures the angular correlation of the two gamma rays is obtained for each instant (coincidence). Due to the hyperfine interactions, the two Γ -ray emissions are perturbed. In a non cubic-metal a probe at a substitutional lattice site experiences an electric field gradient. Using the quadrupole coupling constant ν_Q measured experimentally and the quadrupole moment of the probe nucleus intermediate state, the EFG magnitude can be obtained by equation 1.24, $V_{zz} = (\nu_Q \hbar)/(eQ)$.

1.2.1 PAC sources and experimental details

For PAC measurements one has to choose radioactive nuclear probe isotopes that have two gamma decays. These isotopes are used on a variety of fields, one of them is solid state physics, by using the nuclear experimental methods of condensed matter, such as perturbed angular correlations. Radioactive isotopes useful as sources for PAC probes must have a γ - γ cascade with large anisotropy, and the isomeric level (see Schatz[8]) that decays must have a lifetime between 10 ns and several ms. One of the most used is ^{111}Cd (figure 1.1), because it has the required two gamma decays to measure the angular correlation, from the excited state ^{111m}Cd to the ground state ^{111}Cd , and because it has a suitable half life to discriminate the decays ($t_{\frac{1}{2}} = 84$ ns).

The probe ions can be inserted in the sample by ion implantation, diffusion, activation or directly in the preparation using radioactive reactants. Concerning implantation it is done at The On-Line Isotope Mass Separator, ISOLDE, at CERN. It uses the proton synchrotron booster of CERN to produce radioactive isotopes by fission spallation or fragmentation reactions in a target placed in the proton beam. Here a proton beam ionizes a target, an event which results in production of many different kinds of radioactive isotopes. These isotopes are accelerated and deflected depending on their mass, with magnetic fields, divided to three different lines, so that different isotopes produced from the same target can be used in different experiments. One can select the mass with great accuracy. For example, isotopes of ^{111}Cd are produced from a molten Sn target and then accelerated with a high voltage tension up to 60 kV, on a selected line according to their mass.

After implantation the samples are annealed, to get the atoms and isotopes rearranged from implantation defects, as the temperature is increased. The isotopes move to substitutional lattice sites, and usually stay there after cooling, for adequate temperatures. This makes it possible to use them as local probes at the atomic level. The annealing is done in a convenient atmosphere, O_2 , Ar, air or vacuum for example. The temperature of annealing

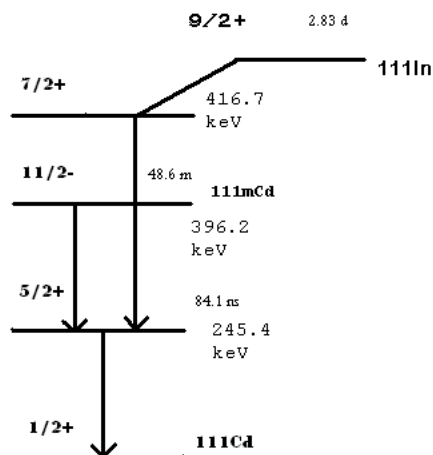


Figure 1.1: Decay of isotope ^{111}In and ^{111m}Cd cascade. Intermediate PAC probe state, with energy $E=254.4$ keV, half life $t_{1/2} = 84.\text{ns}$ and angular momentum $I=5/2$.

varies but for the LaMnO_3 and materials of the same type it is around 700°C for 20 minutes. The implanted sample is then put in the middle of detectors. Detectors for the γ decays are at fixed angles between each other. Usually four detectors measure at fixed angles of 90° and 180° . In this case there are 12 combinations of two detectors. A 6 detector apparatus is also used, with the advantage of measuring more decays. With a six detector setup, that provides the possibility to have more spectra thus measuring more efficiently, 30 combinations of two detectors produce different spectra. This combinations are 6 pairs of detectors at an angle of 180° and 24 at 90° . In TD-PAC (Time dependent PAC) spectroscopy, each combination of two detectors measures coincidence count rate as a function of time. Signals of the two decays are pre amplified and sent to a single-channel analyzer. The time signal of the second decay is delayed, so that the coincidence of γ_1 and γ_2 is measured within a time window. The single channel analyzers must also be calibrated to discriminate the energies of the two decays. With coincidence, new signals are generated, sent to a time-amplitude converter (TAC), that produces an analogical signal with amplitude proportional to the time difference between the start and stop signals. This analogical signal is converted to digital by an ADC and sent to a multichannel analyzer. The data from the SCA is also used to record the spectrum number, by determination of the detectors involved. Further details on the experimental scheme can be found in [8].

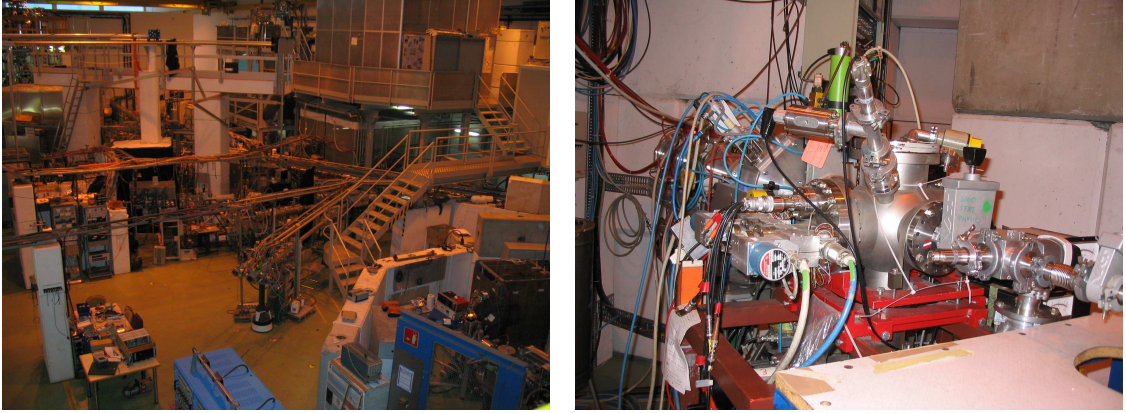


Figure 1.2: Left: ISOLDE Hall. Right: Vacuum chamber where the sample holder is placed and the samples are implanted with radioactive isotopes.

At the solid state physics laboratory at ISOLDE PAC measurements can be made at temperatures from 10 to 1200 K, with several atmospheres (vacuum, air, N₂, Ar,...).

The ratio of signal to noise decreases as $1/\tau_N$, so small decays within experimental resolution are ideal. The lower limit of the time resolution is set by the experimental apparatus and the higher limit is set by signal to noise considerations. The detectors measure real coincidences, between the two decays of the same nucleus, but also accidental coincidences of different nuclei. This accidental coincidences constitute noise because they have no correlation. For a large number of decays or a big lifetime, the signal of correlations is not easily identified. In the particular case of EFG investigations, sources should have a large isomeric quadrupole moment ($Q \geq 0.1b$)². One of the most used probes in PAC is ¹¹¹Cd, which is provided by the source ¹¹¹In, that decays to an excited isomeric state ^{m111}Cd with a γ - γ cascade. Other sources commonly used are ¹⁸¹Hf and ¹⁰⁰Pd, and correspond respectively to the probes ¹⁸¹Ta and ¹⁰⁰Rh.

The time dependence of the angular correlation, described by the perturbation factor, gives complete information of the measurements of PAC[8]. This time dependence corresponds to a rotation of the radiation pattern observed by the two decays.

²1barn = $10^{-28}m^2$ is a unit of area used to express cross sections of scattering processes.

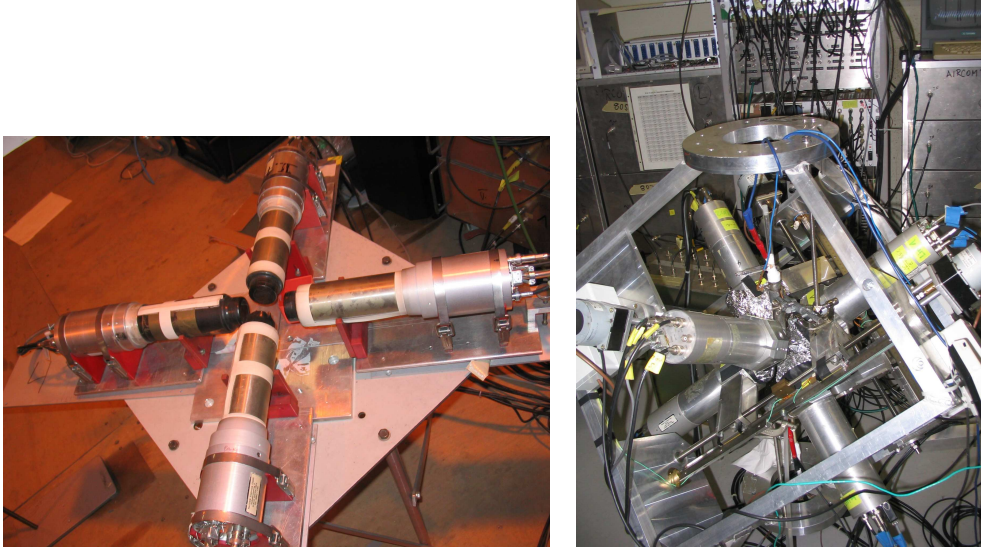


Figure 1.3: Left: System of 4 detectors used for PAC spectroscopy. Right: System of 6 detectors.

1.2.2 Theory and analysis of spectra

The function of coincidence counts of detectors i and j , or differential coincidence count rate, at an angle θ and time t , is

$$N_{ij}(\theta, t) = N_0 \exp\left(\frac{t}{\tau_N}\right) W(\theta, t) + B, \quad (1.34)$$

where B is the random coincidence count rate background and $W(\theta, t)$ is the time dependent angular correlation function. The time dependent angular correlation function rigorous form, can be deduced and the result is

$$W(\mathbf{k}_1, \mathbf{k}_2, t) = \sum_{k_1, k_2, N_1, N_2} A_{k_1}(1) A_{k_2}(2) G_{k_1 k_2}^{N_1 N_2}(t) \frac{1}{\sqrt{(2k_1 + 1)(2k_2 + 1)}} \quad (1.35)$$

$G_{k_1 k_2}^{N_1 N_2}(t)$ is the perturbation factor, the quantity of interest in PAC spectroscopy. Its rigorous form is

$$G_{k_1 k_2}^{N_1 N_2}(t) = \sum_{M_a, M_b} (-)^{2I+M_a+M_b} \sqrt{(2k_1 + 1)(2k_2 + 1)} \\ \times \begin{pmatrix} I & I & k_1 \\ M'_a & -M_a & N_1 \end{pmatrix} \begin{pmatrix} I & I & k_2 \\ M'_b & -M_b & N_2 \end{pmatrix} \langle M_b | \Lambda(t) | M_a \rangle \langle M'_b | \Lambda(t) | M'_a \rangle^*. \quad (1.36)$$

The measurements are easily used to calculate the function of coincidence counts N_{ij} . A function

$$R(t) = \frac{2}{3} \left[\sqrt{\frac{N_{13}(180, t)N_{24}(180, t)}{N_{14}(90, t)N_{23}(90, t)}} - 1 \right] \quad (1.37)$$

can remove time dependence from the decay (e^{t/τ_N} disappears).

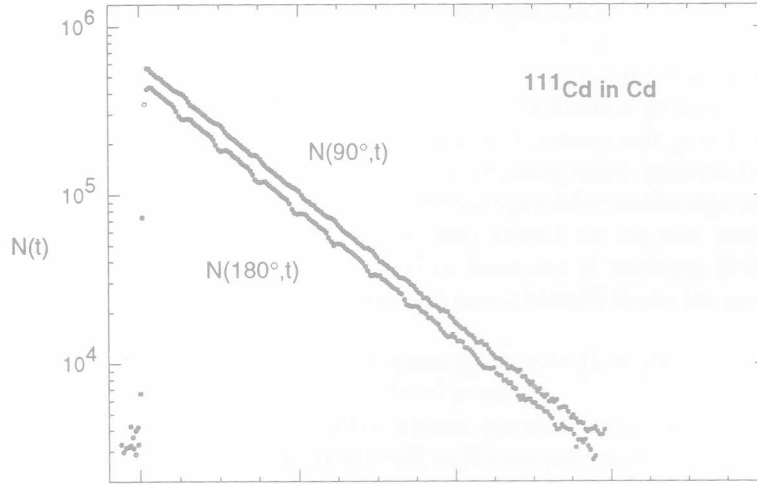


Figure 1.4: PAC spectrum for ^{111}Cd in cadmium metal. Coincidence count rates $N(\theta, t)$ for $\theta = 90^\circ$ and $\theta = 180^\circ$.

For axially symmetric randomly oriented electric field gradients the angular correlation is given by

$$W(\theta, t) = 1 + A_{22}G_{22}(t)P_2(\cos\theta) + \dots \quad (1.38)$$

Neglecting the terms with $k > 2$ the count ratio is given by

$$R(t) = A_{22}G_{22}(t) \quad (1.39)$$

With the perturbation factor determined the hyperfine fields can be calculated. For example, for the case of ^{111}Cd in Cadmium metal, the experimentally $R(t)$ obtained is fitted to a theoretical sum of co-sines:

$$R(t) = A_{22}G_{22}(t) = A_{22} \sum_{n=0}^3 s_{2n} \cos(n\omega_Q^0 t) \quad (1.40)$$

and gives the quadrupole frequencies. Using the quadrupole moment of the ^{111}Cd intermediate state the electric field is calculated with equation 1.24.

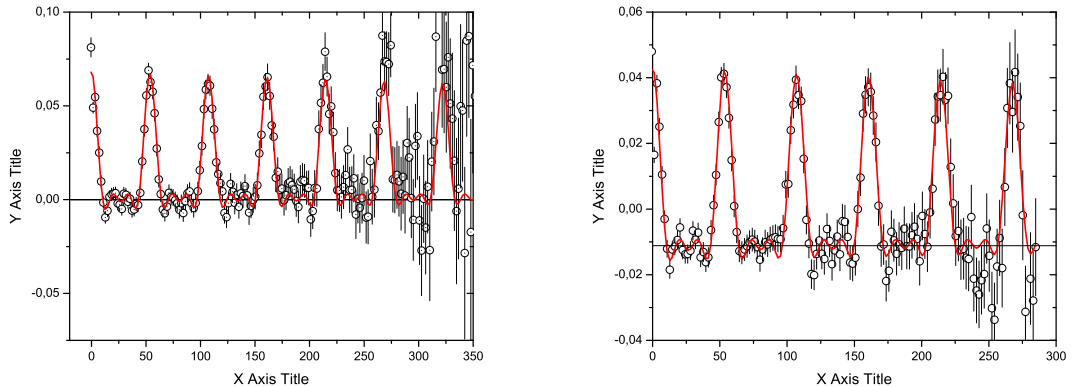


Figure 1.5: Graphics of the count rate $R(t)$ obtained with two machines for ^{111}Cd in Cd metal. The solid line are fitted to the theoretical function (Eq 1.40), to obtain a set of quadrupolar frequencies.

The experimental data are analyzed and fitted according to theory following these rules, with a computer program specific to PAC³. Figures 1.4 and 1.5 give an experimental example of the spectrum obtained for ^{111m}Cd decaying in Cd metal. The coincidence count rates are $N(\theta, t)$, where θ is the angle between the two detectors measuring the coincidence, are plotted on a logarithmic scale. Without perturbation, it should be a straight line. The count-rate ratio $R(t)$ shows that perturbation. In this simple case, this function has a good periodicity and the frequencies are easily taken from the Fourier transform. The spectra of ^{111}Cd implanted in a Cd foil are used to calibrate the experimental setups. More complicated examples for the type of sample commonly study, CaMnO_3 and PrMnO_3 are in figures 1.6 and 1.7.

Typical obtained values reproduced from PAC measurements in the materials analyzed in this thesis are presented in the table. During this thesis I have participated in experiments done at ISOLDE in June/July 2007 where general manganite systems were studied as a function of composition and/or temperature. The data are still being analyzed and are not presented in this thesis.

³Developed by the Instituto Tecnológico Nuclear group at CERN (Dr. Guilherme Correia)

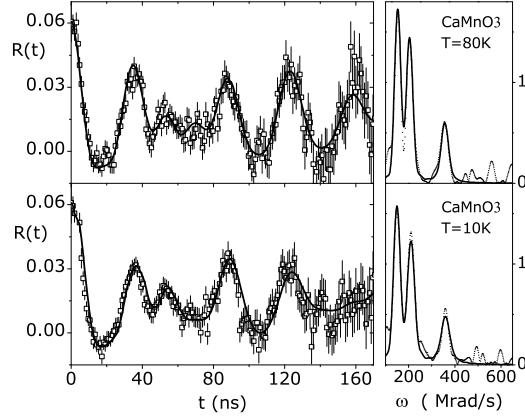


Figure 1.6: Experimental functions $R(t)$ (left) and corresponding Fourier spectra(right) for CaMnO_3 at 80 K(top) and 10K(bottom). Fits to the experimental spectra are the continuous lines over $R(t)$ and the Fourier transform. Taken from [11].

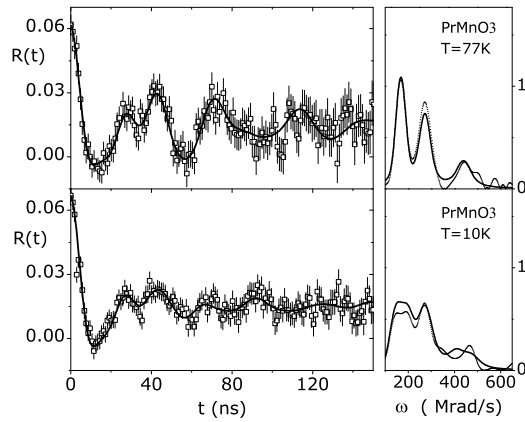


Figure 1.7: Experimental functions $R(t)$ (left) and corresponding Fourier spectra(right) for PrMnO_3 at 77 K(top) and 10K(bottom). Fits to the experimental spectra are the continuous lines over $R(t)$ and the Fourier transform. Taken from [11].

x	$T(K)$	$V_{zz}(V/\text{\AA}^2)$	η
0	77	74.6	0.44
0	10	74.8	0.41
0.05	77	74.4	0.46
0.14	77	73.6	0.46
0.95	77	60.3	0.64
1	80	59.3	0.64
1	10	59.7	0.60

Table 1.1: Low temperature EFG parameters for some samples of the series $\text{Pr}_{1-x}\text{Ca}_x\text{MnO}_3$ and for the compositions $x=0.05, 0.14$ and 0.95 , and for three different low temperatures [11].

Chapter 2

Perovskite type manganese based oxides

2.1 Structure

The particular class of these materials of the form $\text{La}_{1-x}\text{A}_x\text{MnO}_3$ (where A is a divalent alkaline-earth, for example Pr, Ca or Ba) is interesting from the point of magnetic properties and also because these materials share the same basic perovskite structure of many other materials (dielectrics, superconductors, and ferroelectrics). This structural similarities make interesting possibilities for the growth of heterostructures with potential multifunctional applications. A description of this basic structure is presented [12], followed by other important properties of these compounds.

2.1.1 Ideal Perovskite Structure

The ideal (cubic, no distortions) perovskite structure is displayed in the figure 2.1. In the ideal perovskite structure ABO_3 , B is a small cation such as Mn^{3+} or Mn^{4+} , and A is a large cation similar in size to O^{2-} . A manganese ion and the six neighboring oxygen ions form a series of regular octahedra. The elementary perovskite cell contains one formula unit ($Z=1$).

Perovskite transition-metal oxides in general have a variety of interesting properties, such as dielectric, magnetic, optical, and transport properties. It is interesting to point out that the study of ferroelectric perovskite materials of the form ABO_3 has been of great relevance in the last years. First-principles calculations can be used to understand transitions between different structures that are difficult to characterize because the atomic displacements are very small[13]. Different crystallographic structures resolved by X-ray can be discarded or chosen, by comparison with theoretical studies.

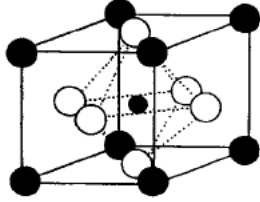


Figure 2.1: Ideal structure ABO_3 , A the atoms at the corners, O the face centered atoms and B at the center.

It is possible to make the calculations for the different structures and check their stability, by the value of the forces obtained in each atomic site.

2.1.2 Crystal structure

In the ideal structure, both cation sites have cubic point symmetry $m\bar{3}m$. However, in the real distorted structures, the point symmetry is much lower. The crystal field influences both the magnetic and electronic properties of oxides. Considering the ideal perovskite structure of figure 2.1, and assuming that it is formed by octahedrally coordinated O^{2-} anions, A^{2+} or A^{3+} cations and B, a small cation placed in the octahedral interstitial site, the ideal ionic radii r_A and r_B can be deduced. $r_A = r_O = 0.140$ nm and $r_B = (2^{1/2} - 1)r_O$. Goldschmidt[14] defined a tolerance factor

$$t = \frac{(r_A + r_O)}{2^{1/2}(r_B + r_O)} \quad (2.1)$$

As t goes away from 1 the ideal structure becomes unstable, because it cannot accommodate the respective ionic sizes. The particular case of $t < 1$ corresponds to B-O bonds under tension and A-B bonds under compression, which results in a cooperative rotation of the BO_6 octahedra and a reduction of the angle of the B-O-B angle from 180° . When t is close to one the rhombohedral structure is usually crystalized, and as t deviates further from one the structure stabilized is orthorhombic, which results from a rotation about the $[110]$ axis. This structure is called O-type. Some ionic radii are listed in the table (2.1.2). In oxides with $0.89 < t < 1.02$ the perovskite structure is stable. These limits can change if a different radii are used from the ones in the table.

O ²⁻	Mn ³⁺	Mn ⁴⁺	Ca ²⁺	La ³⁺
1.40	0.645	0.530	1.34	1.36

Table 2.1: Shannon ionic radii of common elements present in perovskite structure oxides(Å)[15]

The tolerance factor can also be defined with the interatomic distances between the oxygen and the ions at A and B sites:

$$t = \frac{d_{A-O}}{\sqrt{2}d_{B-O}} \quad (2.2)$$

Jahn-Teller effect

In addition to the cooperative rotation of the octahedra MnO₆, another possible deformation of the structure is a cooperative oxygen displacement, deforming the regular octahedra. Some oxygens move towards one neighbor Mn atom and away from the others. With this deformation the so called O'-type structure is stabilized, with superposition of the octahedra rotation and octahedra deformation. This octahedra deformation is called the Jahn-Teller deformation, and occurs in the presence of a particular electronic configuration of some ions.

Considering the free Mn³⁺ (3d⁴) and Mn⁴⁺ (3d³) ions, the d orbitals (d_{xy}, d_{yz} and d_{x²-y²}) are degenerate in energy. However, if the Mn ion is at the center of a oxygen octahedra the crystal field splits the d orbitals in two subgroups, e_g (d_{x²-y²} and d_{z²}) and t_{2g} (d_{xy}, d_{yz}, d_{zx}). The e_g orbitals, directed towards the O²⁻ neighbor ions, have higher energy because of electrostatic repulsion. The orbitals d_{xy}, d_{yz} and d_{zx} which have their lobes oriented between the oxygen neighbors and a group of two e_g orbitals, have a lower energy.

If the ion is Mn³⁺, four electrons occupy the d orbitals, three in the t_{2g} orbitals and one electron occupies the e_g orbitals. Mn³⁺ and Mn⁴⁺ usually have electrons with parallel spin, according to Hund's rules¹. Since a very high energy is necessary to put this electron in the higher energy orbitals, when compared with the crystal field splitting, the octahedra deforms. The defor-

¹Two electrons cannot share the same quantum number in the same system, due to the Pauli exclusion principle. Hund's second rule states that the lowest energy atomic state is the one which maximizes the sum of the S values for all of the electrons in the system, maximizing the number of unpaired electrons. This is usually the lowest energy state, because it results in a larger average distance between two electrons, reducing electron-electron repulsion.

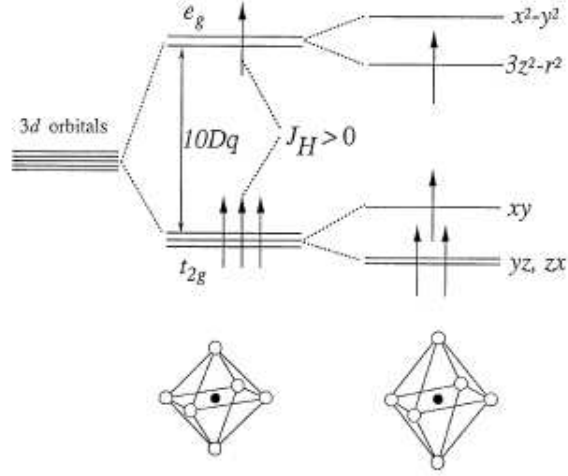


Figure 2.2: Field splitting of the degenerate atomic 3d levels into lower t_{2g} and higher e_g levels. The particular Jahn-Teller distortion lifts each degeneracy as shown, for the case of Mn^{3+} [16].

mation (Jahn-Teller distortion) lifts the degeneracy of the orbitals, making the energy jump necessary for the extra electron smaller.

This strong electron lattice coupling is present generally in manganite systems. Although most manganites are derived from the ideal structure, few have precisely that structure, because the atoms are displaced from their ideal positions when $t' \neq 1$. To accommodate misfit in ionic sizes or electronically induced structural deformations a structure with lower symmetry is formed. Usually an orthorhombic or rhombohedral phase is formed, and the unit cell is larger than the ideal cubic structure unit cell. The orthorhombic structure for example, is described by a cell with four unit formulas ($Z=4$). The parameters of the O-type orthorhombic structure (a_O , b_O and c_O) are related to the cubic parameter a_P by the relations $a_O \approx \sqrt{2}$, $b_O \approx a_P\sqrt{2}$ and $c_O = 2a_P$. Different relations between these parameters may occur depending on the type of orthorhombic structure formed. For the O-type structure $a_O\sqrt{2} \leq c_O \leq b_O\sqrt{2}$, and for the O'-type structure $c_O \leq a_O\sqrt{2} \leq b_O\sqrt{2}$.

2.1.3 Colossal magnetoresistance

Magnetoresistance is a property of materials that consists on the change of the electric resistivity in the presence of a magnetic field. Conventional magnetoresistant materials can change their resistivity over 5%. With layers of

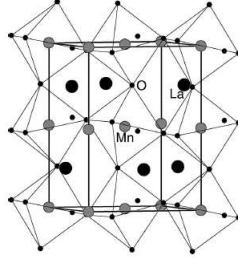


Figure 2.3: The GdFeO_3 -type crystal structure of LaMnO_3 , an orthorhombically distorted perovskite-type structure.

materials it is possible to obtain large values of magnetoresistance, the so called giant magnetoresistance[17, 18]. In 1993 it was shown that manganese based oxides presented a resistivity change by several orders of magnitude[1]. This magnetoresistance effect, exhibited in mixed-valence manganites, is so large compared with the rest of materials that it was dubbed colossal magnetoresistance. Since then the research on these class of oxides has increased rapidly. Colossal magnetoresistive materials are technologically important for many magnetic applications including magnetic storage devices for recording media and magnetoresistive sensors.

2.1.4 Double exchange and super exchange

The magnetoresistance of mixed-valence manganites was initially explained by the ferromagnetic double exchange interaction[5]. This corresponds to an electron transfer from the Mn^{3+} ions to the adjacent Mn^{4+} . This exchange happens by simultaneous transfer of the e_g electron from the Mn^{3+} ion to the oxygen between the Mn ions involved, and from this oxygen to the Mn^{4+} ion. Because of the strong atomic Hund coupling, double exchange is favored when the transfer electron has spin parallel to the atomic spins. This corresponds to a ferromagnetic arrangement of Mn ions, and correlates the magnetism and resistivity, giving a reasonable explanation for the phenomenon of magnetoresistance on these materials. As opposed to double

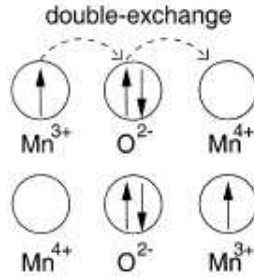


Figure 2.4: Sketch of the double exchange mechanism, which involves two Mn ions and one O ion.

exchange, super exchange is an interaction between two Mn^{3+} ions. In this case there is not an electron transfer between this two ions, as they both have one electron in the e_g orbital, and it would require energy to put a second electron in the e_g orbital. In this case the Pauli exclusion principle rules the interaction, the e_g electron of each ion has opposed spin to an electron in the 2p oxygen orbitals. This results in antiferromagnetic coupling between the two Mn ions. The interaction between two Mn^{4+} ions is also antiferromagnetic super exchange, no charge transfer occurs. Accordingly, pure compounds such as LaMnO_3 and CaMnO_3 have antiferromagnetic insulating ground states. Substituting a portion of La by a divalent ion like Ca^{2+} , in a compound of the form $\text{La}_{1-x}\text{Ca}_x\text{MnO}_3$, for example, results in the appearance of an equivalent amount of Mn^{4+} , which favors ferromagnetism via the $\text{Mn}^{3+}\text{-Mn}^{4+}$ double exchange interaction. This competition between double exchange and super exchange is now considered insufficient to explain the states of manganites.

2.1.5 Other properties

Various spin arrangements are possible in these materials. Several arrangements labeled A,B,C,D,E,F,G are possible in manganites, and combinations of these arrangements, for example CE. Some possible modes for the Mn ions on the perovskite structure are presented in figure 2.5. There are also charge

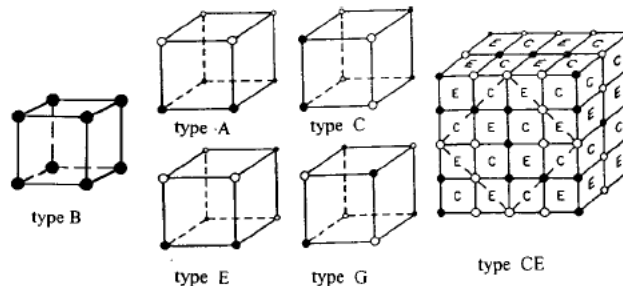


Figure 2.5: Some possible modes for the B-site cations in the perovskite structure (solid and open circles represent two antiferromagnetic sublattices) [12]

ordered phases in manganites, such as the CE-type antiferromagnetic ordering in half doped manganites. Since the estimation of the Curie temperature on manganites using double exchange gives a wrong T_C by a large factor [19], it is argued that DE does not explain the complex phenomena inherent to this material. Nowadays it is accepted that there are several different interactions competing: magnetic interaction between Mn spins, electron-phonon coupling, electronic repulsion and electronic condensation energy, to name a few. The state of mixed-valence manganites is therefore intrinsically inhomogeneous, and that is favorable to phase separation. Nano domains of different phases were confirmed by experimental results [20], and are believed to be of great importance to the colossal magnetoresistance, by a percolation process. Normally ferromagnetic metallic and charge ordered insulating clusters are formed, but several phases can be involved. To conclude, phase diagrams of these materials obtained by varying either the temperature or the composition x in the case of mixed-valence manganites $R_xA_{1-x}MnO_3$ are very rich in different magnetic and electronic states. The diagram of $La_{1-x}Ca_xMnO_3$ is in the figure 2.1.5. Another example of a phase diagram is shown in the case $Pr_{1-x}Ca_xMnO_3$, figure 2.1.5.

We now describe in detail the structure of the La end-member, with La as the only rare-earth, $LaMnO_3$.

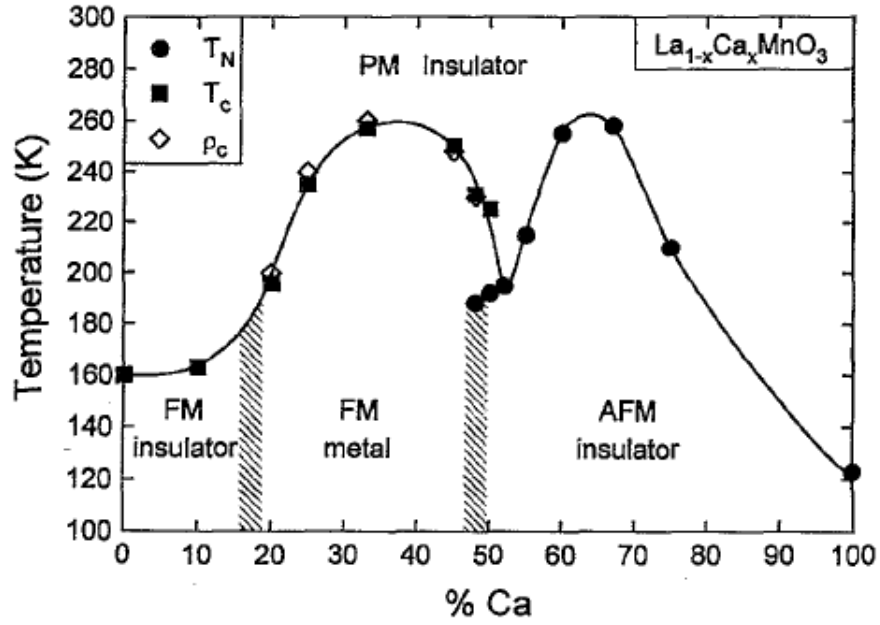


Figure 2.6: Example of the complex phase diagrams obtained by varying composition and temperature of manganites, in this case with $\text{La}_{1-x}\text{Ca}_x\text{MnO}_3$ [21]

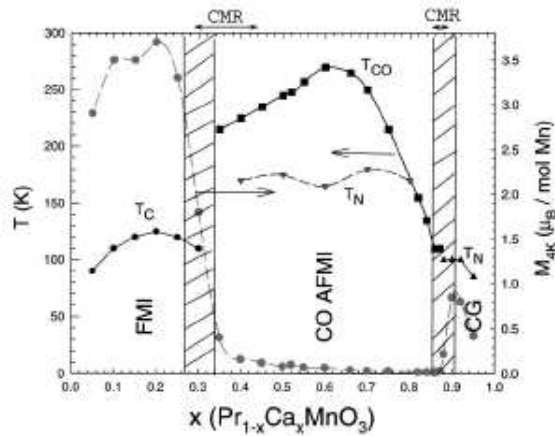


Figure 2.7: Example of the complex phase diagrams obtained by varying composition and temperature of manganites, in this case with $\text{Pr}_{1-x}\text{Ca}_x\text{MnO}_3$ [22]

LaMnO₃

The ground state stoichiometric crystal LaMnO₃ is stabilized in the O'-type orthorhombic structure (GdFeO₃-type structure), space group Pbnm (equivalent to space group Pnma with a different choice of axes, a, b, c in Pbnm become c, a, b in Pnma.) with $a = 5.54$, $b = 5.75$ and $c = 7.70\text{\AA}$. It has a quadrupled unit cell, comprising four formula units, with parameters (a, b, c) equal to $(\sqrt{2}a_P, 2a_P, a_P\sqrt{2})$. The Mn-O-Mn bond angles are about 155° . The MnO₆ octahedron is Jahn-Teller distorted in such a way that the long and short Mn-O bonds lie in the a-b plane. Mn-O bond lengths are 2.18\AA and 1.91\AA in plane and 1.96\AA along the c axis. The in-plane Mn-Mn distance is 3.99\AA . The interplane separation along the c axis which corresponds to the intermediate Mn-O distance is a little shorter, 3.85\AA . At a temperature of about 1020 K, the orthorhombic distortion disappears and the compound becomes rhombohedral (quasicubic) with the R-type LaAlO₃ structure. There is also an O'→O orthorhombic transition at 940 K. The tolerance factor is $t_P = \frac{(R_{La}+R_O)}{[\sqrt{2}(R_{Mn}+R_O)]}$, where R_{La} , R_{Mn} , and R_O are the ionic radii for La, Mn, and O, respectively, giving $t_P = 50.947$ for LaMnO₃. Early theoretical work focused on the undistorted perovskite structure and it was found that it cannot produce the correct insulating ground state for LaMnO₃. [23]

Chapter 3

Concepts of electronic structure calculations

3.1 Density functional theory

In general it is not possible to obtain the exact solution to the quantum many body problem, so that approximations have to be used. One of the most popular approaches in condensed matter physics to solve the many-electrons problem of a crystal is density functional theory(DFT)[24, 25], which is the approach behind the computer program used in this work, Wien2k[7]. It has been employed with success to predict superconductive and magnetic properties of solids, and in chemistry, to calculate detailed reaction mechanisms, for example. To understand the basic concepts of this theory an explanation starting with wave mechanics is useful.

3.1.1 Wave Function

The Born-Oppenheimer approximation usually covers problems of interest in electronic structure. It simplifies the problem by keeping the nuclei fixed, entering the hamiltonian merely as sources of an external potential. It consists in two assumptions, the first is that the motion of nuclei and electrons are decoupled, so that the wave function can be written as a product of two wave functions, one electronic and one nuclear. The electronic depends only on the nuclear coordinates, since it is assumed that a change in nuclei coordinates translates instantaneously into a change in the motion of electrons. It is usually valid, since nuclei have typically 2000 times or higher more mass than the electrons, and it enables us to describe the behavior of a system

with the time-independent Schrödinger equation.

$$\hat{H}\Psi = E\Psi \quad (3.1)$$

The other assumption is treating the nucleus as classical particles, since they are so massive, and thus obey Newton's laws. In the Born-Oppenheimer approximation, and disregarding relativistic effects (in Ry atomic units¹),

$$\hat{H} = \hat{T} + \hat{V}_{ne} + \hat{V}_{ee} = \sum_{i=1}^N \left(-\frac{1}{2}\nabla_i^2\right) + \sum_{i=1}^N v(\mathbf{r}_i) + \sum_{i<j}^N \frac{1}{r_{ij}}. \quad (3.2)$$

\hat{T} , \hat{V}_e and \hat{V}_{ee} are the kinetic energy of electrons, the potential on the electrons due to the fixed nuclei and the electron-electron interaction, respectively.

$$v(\mathbf{r}_i) = - \sum_{\alpha} \frac{Z_{\alpha}}{r_{i\alpha}} \quad (3.3)$$

is the external potential acting in the electron i due to the nuclei of charges Z_{α} . When a system is in the state Ψ , each particular measurement of the energy gives one of the eigenvalues of \hat{H} , and

$$E[\Psi] \geq E_0, \quad (3.4)$$

i.e. the energy computed from any Ψ is an upper bound to the true ground state energy E_0 . To find the true ground state Ψ_0 for which $E[\Psi_0] = E_0$, we need to minimize the energy,

$$E_0 = \min E[\Psi] \quad (3.5)$$

so that the Schrödinger equation corresponds to the variational principle

$$\delta E[\Psi] = 0. \quad (3.6)$$

There are a number of methods used to solve the many-body electron problem based on the expansion of the wave function in Slater determinants, such as the Hartree-Fock method. The problem with this approach is that each determinant requires $N!$ terms. Because the electrons are interacting with each other and there are $\approx 10^{23}$ electrons in crystals, the wave-function must consist of a huge number of terms. It requires great computational efforts

¹In the system of Rydberg atomic units, six physical constants are unit: the charge and mass of the electron, Bohr radius and the absolute value of the electric potential energy in the ground state of hydrogen, Planck's constant, and the constant for Coulomb's law ($\frac{1}{4\pi\epsilon_0}$).

even for small systems, and the reason is that it depends on the complicated N-electron wave function $\Psi(\mathbf{x}_1, \mathbf{x}_2, \dots, \mathbf{x}_N)$, with $3N$ degrees of freedom.

With density functional theory the calculational scheme uses instead of this wave function the much simpler electronic density $\rho(\mathbf{r})$ which has only 3 degrees of freedom, it depends only on the position. Despite this change of variable, DFT is in principle an exact theory. In practice it is not possible to have an exact expression to the exchange correlation potential (defined in Eq. 3.11), since it depends on the approximation used to define the this functional (section 3.1.5).

3.1.2 Hohenberg-Kohn theorems

Hohenberg and Kohn legitimized the use of the electronic density as a basic quantity[24, 25], with two theorems: The first theorem states that the external potential $v(\mathbf{r})$ is determined, within a trivial additive constant, by the electron density $\rho(\mathbf{r})$. Since the density determines the number of electrons, it follows that it also determines the ground-state wave function and all the other electronic properties of the system.

Then we have

$$E_\nu[\rho] = T[\rho] + V_{ne}[\rho] + V_{ee}[\rho] = \int \rho(\mathbf{r})v(\mathbf{r})d\mathbf{r} + F_{HK}[\rho]. \quad (3.7)$$

F_{HK} is the Hohenberg-Kohn functional, defined as

$$F_{HK}[\rho] = T[\rho] + V_{ee}(\rho), \quad (3.8)$$

and

$$V_{ee}[\rho] = J[\rho] + \text{nonclassical term}, \quad (3.9)$$

is the electron-electron interaction, where $J[\rho]$ is the classical repulsion

$$J[\rho] = \frac{1}{2} \int \int \frac{1}{r_{12}} \rho(\mathbf{r}_1)\rho(\mathbf{r}_2)d\mathbf{r}_1d\mathbf{r}_2, \quad (3.10)$$

The non-classical term is the major part of the exchange-correlation energy. The exchange-correlation energy is defined as the interacting part of the electronic kinetic energy plus the non classical part of the electron-electron interaction.

$$E_{xc}[\rho] = T[\rho] - T_S[\rho] + V_{ee}[\rho] - J[\rho], \quad (3.11)$$

where $T_S[\rho]$ is the non-interacting part of the electronic kinetic energy, and $T[\rho] - T_S[\rho]$ is presumably fairly small.

The second Hohenberg-Kohn theorem provides the energy variational principle: for a trial density $\tilde{\rho}(\mathbf{r})$, such that $\tilde{\rho}(\mathbf{r}) \geq 0$ and $\int \tilde{\rho}(\mathbf{r}) d\mathbf{r} = N$,

$$E_0 \leq E_\nu[\tilde{\rho}] \quad (3.12)$$

where $E_\nu[\tilde{\rho}]$ is the energy functional of (3.7). This is analogous to the variational principle for wave functions (3.4).

3.1.3 Thomas-Fermi model

The Thomas-Fermi Model, developed before the Hohenberg-Kohn theorems, is conceptually similar to the density functional theory, and is responsible for the development of DFT. In this model the kinetic energy is a functional of the density, combined with the classical electron-electron and electron-nuclear attractions to give the total energy. This model works only for simple cases, since it neglects the exchange-correlation energy. Some developments were made to include an exchange energy functional by Dirac[26], but it still neglects the correlation energy completely.

3.1.4 Kohn-Sham method

The most common formulation of DFT, the Kohn-Sham method[25], uses an analogy of the functional F_{HK} (3.8) for a corresponding non-interacting system, with the Hamiltonian

$$\hat{H}_S = \sum_i \left(-\frac{1}{2}\nabla_i^2\right) + \sum_i^N v_S(\mathbf{r}_i) \quad (3.13)$$

in which there are no electron-electron repulsion terms. For this system the ground-state density is exactly ρ , and there is an exact ground-state wave function

$$\Psi_S = \frac{1}{\sqrt{N!}} \det[\psi_1 \psi_2 \dots \psi_N] \quad (3.14)$$

where the ψ_i are the N lowest eigenstates of the one-electron hamiltonian \hat{h}_S :

$$\hat{h}_S \psi_i = \left[-\frac{1}{2}\nabla^2 + v_S(\mathbf{r})\right] \psi_i = \epsilon_i \psi_i \quad (3.15)$$

and the kinetic energy is $T_S[\rho]$. Using this set of orbital functions with the variational problem of Hohenberg-Kohn, a set of equations can be derived, the KS orbital equations:

$$\left[-\frac{1}{2}\nabla^2 + v_{eff}\right] \psi_i = \epsilon_i \psi_i \quad (3.16)$$

$$v_{eff} = v(\mathbf{r}) + \int \frac{\rho(\mathbf{r}')}{|\mathbf{r} - \mathbf{r}'|} d\mathbf{r}' + v_{xc}(\mathbf{r}) \quad (3.17)$$

These equations must be solved in a self-consistent way(iteratively). To summarize, one usually starts with a guess for the electronic density, calculates v_{eff} , and solves for ψ_i . The orbitals ψ_i give the new density, and we find a new effective potential, repeating this cycle until convergence is reached. This procedure is illustrated in the figure3.1.4.

3.1.5 Approximations

The functionals for exchange and correlation are not defined in a closed form. However approximations permit the calculations of physical quantities to be quite accurate. The simplest and most widely known approximation is the linear density approximation(LDA). It assumes that the functionals depend only on the density. With this approximation,

$$E_{xc}^{LDA} = \int \rho(\vec{r}) \epsilon_{xc}(\vec{r}) d\vec{r} \quad (3.18)$$

the assumption is that the exchange-correlation due to a particular energy could be found by dividing the material in infinitesimally small volumes, each with a constant density. LDA is expected to work well for systems with slowly varying densities, and surprisingly it performs reasonably well for other cases too.

The local spin density approximation(LSDA), generalizes LDA for the inclusion of spin, needed for magnetic systems. With this scheme, the spin densities $\rho_\sigma(r)$ are the key quantities. The total energy of the system is obviously a function of these quantities:

$$E_{tot}(\rho_\uparrow, \rho_\downarrow) = T_s(\rho_\uparrow, \rho_\downarrow) + E_{Ne}(\rho_\uparrow, \rho_\downarrow) + E_{xc}(\rho_\uparrow, \rho_\downarrow) + E_{NN}, \quad (3.19)$$

where E_{NN} is the repulsive Coulomb energy of the fixed nuclei and the electronic contributions T_s , E_{ee} and $E_{Ne}(\rho_\uparrow, \rho_\downarrow)$ are, respectively, the kinetic energy of non-interacting electrons, the electron-electron repulsion and the exchange-correlation energies. Within LSDA, E_{xc} can be written in terms of a local exchange-correlation energy μ_{xc} times the total electron density, just like the LDA, and the equivalent equation is

$$E_{xc}^{LSDA} = \int \mu(\rho_\uparrow, \rho_\downarrow) [\rho_\uparrow + \rho_\downarrow] dr. \quad (3.20)$$

,

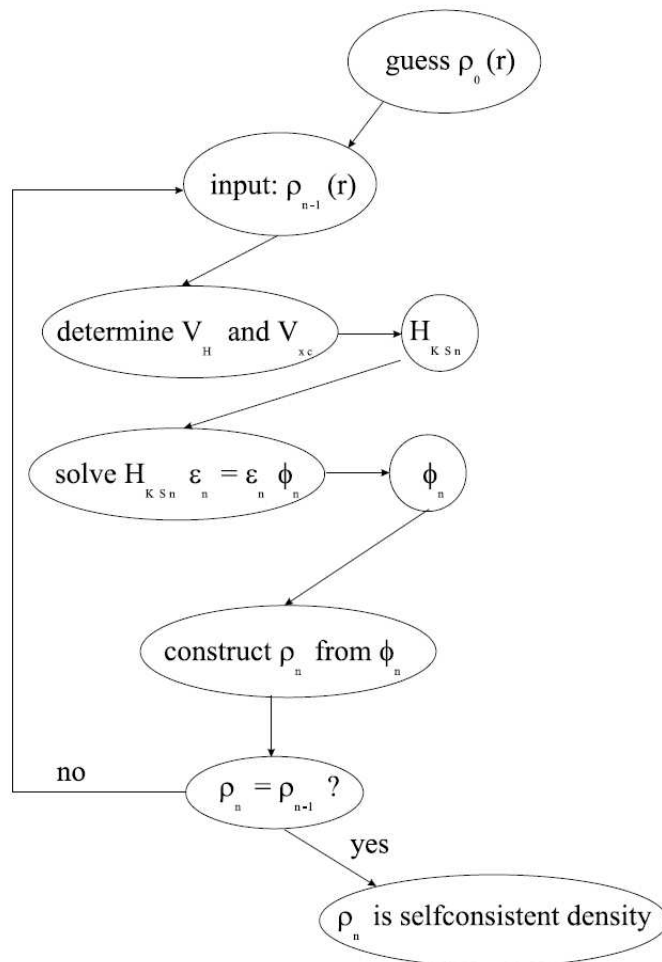


Figure 3.1: Flow Chart for the n^{th} iteration in the selfconsistent procedure to solve the Kohn-Sham equations[27].

and the particular form of μ_{xc} is an assumption also made. Several forms can be found in the literature.

Then, E_{xc} can be minimized by means of the variational principle, introducing orbitals ψ_{ik}^σ such that

$$\rho_\sigma(r) = \sum_{i,k} n_{i,k}^\sigma |\psi_{ik}^\sigma(r)|^2, \quad (3.21)$$

where $n_{i,k}^\sigma$ are occupation numbers such that $0 \leq n_{i,k}^\sigma \leq 1/\omega_k$, where ω_k is the symmetry-required weight of point k . The variation of E_{tot} gives the Kohn-Sham equations (in Ry atomic units):

$$[-\nabla^2 + V_{Ne} + V_{ee} + V_{xc}^\sigma] \psi_{ik}^\sigma(r) = \epsilon_{ik}^\sigma(r) \psi_{ik}^\sigma(r). \quad (3.22)$$

Now this equation is solved self-consistently in an iterative process, since finding the Kohn-Sham orbitals requires the knowledge of the potentials, which themselves depend on the (spin-)density and thus on the orbitals again.

Recently, new approximations beyond the LSDA have been made. The logical step needed to improve LDA is to make the exchange-correlation not only dependent on the local density but also on the density of the neighboring volumes. This is achieved by adding gradient terms of the electron density to the exchange-correlation energy or its corresponding potential. This approximation then is called generalized gradient approximation(GGA). GGA is still local, although it also takes into account the gradient of the density, it is the density at the same coordinate. GGA is described by an expression of the form

$$E_{xc}[\rho^\alpha(r), \rho^\beta(r)] = \int dr f[\rho^\alpha(r), \rho^\beta(r), \nabla\rho^\alpha(r), \nabla\rho^\beta(r)] \quad (3.23)$$

α and β are the indexes for different spins, when performing spin-polarized calculations. One recent form of GGA by Perdew, Burke and Ernzerhof (PBE) (1996)[28] has proven to be the best one for most cases, and is the most widely used by physicists. This is the approximations that I use by default in all the calculations in this work. There are recent versions of GGA, such as meta-GGA by Perdew et al (1999)[29] and Tao et al (2003)[30] but self-consistency is not yet easily achieved in such models. The disadvantages of this approximation are the number of different versions, because of the freedom to include the gradient, and that some versions are not strict ab initio models, and some experimental values are needed.

To solve the equation (3.1) with density functional theory as well as other methods we need a suitable basis set to express the orbitals ψ_{ik} . In theory this set should be infinite, in practice a limited set of functions is used. By

choosing the size of the basis set, we are determining the number of eigenvalues to be solved, since solving the Kohn-Sham equations means solving an eigenvalue problem. Obviously the larger basis set corresponds to more time consuming problems, as bigger matrixes have to be diagonalized. Some basis sets can be defined that are more efficient, because they provide good convergence with a smaller size and thus reduced time. However such efficient sets are usually biased, because they solve some cases very well and quickly, but not acceptable in other situations. The challenge here is to find basis sets that are both efficient and unbiased. In the next section some basis sets for the implementation of density functional theory will be described.

3.1.6 Basis sets

Pseudopotentials[31]

A plane wave expansion is a mathematically simple way to describe a basis set. Plane waves are functions of the form

$$f(\mathbf{r}) = e^{i\mathbf{k}\cdot\mathbf{r}}, \quad (3.24)$$

where \mathbf{k} is any vector of the first Brioullin zone. An eigenfunction $\psi_{\mathbf{k}}^n$ of a periodic hamiltonian, can be expanded in a plane wave basis with an infinite set of coefficients $c_{\mathbf{k}}^n$:

$$\Psi_{\mathbf{k}}^n = \sum_{\mathbf{k}} c_{\mathbf{K}}^{n,\mathbf{k}} e^{i(\mathbf{k}+\mathbf{K})\cdot\mathbf{r}} \quad (3.25)$$

\mathbf{K} is any vector of the reciprocal lattice. The basis functions are:

$$|\phi_{\mathbf{K}}\rangle = e^{i(\mathbf{k}+\mathbf{K})\cdot\mathbf{r}}. \quad (3.26)$$

The basis depends on \mathbf{k} , so that different \mathbf{k} correspond to a different basis. It is not possible to use an infinite basis set, the set must be limited. With plane waves, this is done by limiting the set to a maximum value of K , K_{max} , corresponding to a sphere with radius K_{max} centered at the origin of the reciprocal space. The energy corresponding to this value is called the cutoff energy, $E = \frac{\hbar^2 K_{max}^2}{2m_e}$. In the region of small radius, close to nucleus, the wave function needed to describe the electronic state is very steep or oscillates a lot, making it necessary, if one wants to use plane waves, to use a large number. In fact except for simple cases this number is so large that is not manageable even with today's computers. For this reason, one method used consists in the inclusion of a pseudopotential. This is a potential which gives a smoother wave function close to the nucleus, making only a few plane wave

functions needed to describe it. This is acceptable because the inner core of electrons are shielded from the outer electrons, which react with other atoms. However, alternatives to this method can be made more efficient. The greater disadvantage of this implementation in this study is the following: the region of interest when calculating hyperfine fields is the one closer to the nucleus, thus making the the pseudopotentials inappropriate to the calculations of electric field gradients.

Augmented Plane Waves(APW)[32]

A viable alternative to the pseudopotentials would be to divide the space in two regions. Electrons bound to the nucleus like if they were in a free atom are called core states, and the ones that participate in chemical reactions with other atoms are the valence states. Since the core electrons behave more or less like they were in a free atom, shielded from interacting with exterior atoms, the region close to the nucleus can be described by an atomic-like wave function, with the use of spherical harmonics. Space will be divided in spheres for the nucleus and inner electrons, called muffin-tin spheres(call it S_α), and the remaining space called the interstitial region(call it I). In the interstitial region plane waves are used. Plane waves are the eigenfunctions of a hamiltonian with zero potential, so this assumes that electrons in the interstitial regions.

This constitutes the augmented plane wave basis set, and the basis functions $\Phi_{\mathbf{K}}$ for the expansion of $\psi_{\mathbf{k}}$ are defined as

$$\Phi_{\mathbf{K}}^{\mathbf{k}} = \begin{cases} \frac{1}{\sqrt{V}} e^{i(\mathbf{k}+\mathbf{K})\mathbf{r}} & \mathbf{r} \in \mathbf{I} \\ \sum_{l,m} A_{l,m}^{\alpha,\mathbf{k}+\mathbf{K}} u_l^\alpha(r', E) Y_m^l(\hat{r}') & \mathbf{r} \in S_\alpha \end{cases}$$

Plane waves in the interstitial region are augmented by atomic-like functions in the muffin tin spheres. \mathbf{k} and \mathbf{K} keep their previous meaning, α is the index of the muffin-tin spheres and $r' = r - r_\alpha$ is the position given with respect to the center of each sphere, θ and ϕ are the spherical coordinates specifying the direction of r' . The u_l^α are solutions for the radial part of the Schrödinger equation for a free atom α at an energy E . Since the atoms are not free, they are just serving in this case as parts of the basis functions, being non physical. $A_{lm}^{\alpha,\mathbf{k}+\mathbf{K}}$ are parameters defined by the requirement that the two sets of functions are not discontinuous, give the same wave functions on the surface of the sphere. This is achieved by expanding the plane wave in spherical harmonics:

$$\frac{1}{\sqrt{V}} e^{i(\mathbf{k}+\mathbf{K})\mathbf{r}} = \frac{4\pi}{\sqrt{V}} e^{i(\mathbf{k}+\mathbf{K})\mathbf{r}_\alpha} \sum_{l,m} i^l j_l(\mathbf{k} + \mathbf{K}|\mathbf{r}|) Y_m^{l*}(\mathbf{k} + \mathbf{K}) Y_{lm}^{\theta\phi} \quad (3.27)$$

The number of terms contained in this equation is infinite, in principle, and to match the two regions the number of values $A_{lm}^{\alpha, \mathbf{k}+\mathbf{K}}$ are infinite. In practice one truncates to some value l_{max} . The cut-off for the plane waves (K_{max}) and for the angular functions (l_{max}) are of comparable quality if the number of nodes per unit of length is identical. This yields the condition $R_{max}K_{max} = l_{max}$. It has some disadvantages :in order to describe an eigenstate accurately with APW's, one has to set E equal to the eigenvalue (or band energy) of that state. But since that is the value it tries to determine, we are forced to start with a guessed value for it and take it as E. The APW is also much slower than than the pseudopotential method, because whereas in pseudopotential one diagonalization of the secular matrix gives all the eigenvalues, with APW one diagonalization is needed for every eigenvalue. In practice this method is not used anymore, but its exposition here is important to introduce the next two methods.

LAPW[33]

The APW method needs a guessed value of the unknown energy of the eigenstate $E = \epsilon_{\mathbf{k}}^n$ to determine $u_l^\alpha(r', E)$, which will be used to calculate that same energy. The linear augmented plane wave (LAPW) method eliminates this difficulty, by calculating $u_l^\alpha(r', \epsilon_{\mathbf{k}}^n)$ from known quantities. Using a Taylor expansion around an energy E_0 ,

$$u_l^\alpha(r', \epsilon_{\mathbf{k}}^n) = u_l^\alpha(r', E_0) + (E_0 - \epsilon_{\mathbf{k}}^n) \frac{\partial u_l^\alpha(r', E)}{\partial E} \Big|_{E=E_0} + O(E_0 - \epsilon_{\mathbf{k}}^n)^2 \quad (3.28)$$

For a fixed E_0 , the substitution of the first two terms of the expansion on the APW equations gives the LAPW.

$$\Phi_{\mathbf{K}}^{\mathbf{k}}(\mathbf{r}) = \begin{cases} \frac{1}{\sqrt{V}} e^{i(\mathbf{k}+\mathbf{K})\mathbf{r}} & \mathbf{r} \in \mathbf{I} \\ \sum_{l,m} \left(A_{l,m}^{\mathbf{k}+\mathbf{K}} e_l^{alpha}(r', E_0) + B_{l,m}^{\alpha, \mathbf{k}+\mathbf{K}} u_l^\alpha(r', E_0) \right) Y_m^l(\hat{r}') & \mathbf{r} \in \mathbf{S}_\alpha \end{cases}$$

Now the difference $E_0 - \epsilon_{\mathbf{k}}^n$ is unknown and to determine it one has to use a second coefficient $B_{lm}^{\alpha, \mathbf{k}+\mathbf{K}}$. To determine both coefficients A and B the sphere boundary must match the functions of the sphere and plane wave both in value and in slope. For example, if we want to

Imagine we want to describe an eigenstate $\psi_{\mathbf{k}}^n$ that has predominantly p-character ($l = 1$) for atom α . This means that in its expansion in LAPW's, the $A_{(l=1)m}^{\alpha, \mathbf{k}+\mathbf{K}}$ are large. It is therefore advantageous to choose E_0 near the center of the p-band. In this way, the $O(E_0 - \epsilon_{\mathbf{k}}^n)$ -term in equation 3.28 will remain small, and cutting after the linear term is certainly allowed. We can repeat

this argument for every physically important l (s-, p-, d- and f-states, i.e. up to $l = 3$) and for every atom. As a result, we should not choose one universal E_0 , but a set of well-chosen $E_{1,l}^\alpha$ up to $l = 3$. (the meaning of the index '1' will become clear).

Taking this into account, the final definition of LAPW is:

$$\Phi_{\mathbf{K}}^{\mathbf{k}}(\mathbf{r}) = \begin{cases} \frac{1}{\sqrt{V}} e^{i(\mathbf{k}+\mathbf{K})\mathbf{r}} & \mathbf{r} \in \mathbf{I} \\ \sum_{l,m} \left(A_{l,m}^{\mathbf{k}+\mathbf{k}} e_l^\alpha(r', E_{1,l}^\alpha) + B_{l,m}^{\alpha,\mathbf{k}+\mathbf{K}} u_l^\alpha(r', E_{1,l}^\alpha) \right) Y_m^l(\hat{r}') & \mathbf{r} \in \mathbf{S}_\alpha \end{cases}$$

$R_{mt}K_{max}$ and basis size

The cutoff parameter K_{max} , which was determined to be a good quantity to judge the accuracy in a pseudopotential calculation, is also a valuable indicator for APW and LAPW, but a better yet quantity for LAPW is $R_\alpha^{min} K_{max}$, the product between the smallest muffin tin radius and K_{max} . The increase of the muffin tin radius means that a plane wave can move farther away from the nucleus. Less plane waves are needed to describe the remaining parts of the wave function, that will be smoother, because it is farthest from the nucleus. An increase of R_α permits reducing K_{max} maintaining the same accuracy. If the product $R_{min}K_{max}$ remains constant the accuracy of different calculations is comparable. A larger R_{min} reduces the computer time maintaining the same accuracy, because it allows the increase of K_{max} , and K_{max} controls the size of the matrices whose diagonalization is very demanding. However, care must be taken with increasing R_{min} , because the spherical harmonics are not appropriate for the description of wave functions far away from the nuclei. With Wien2k[7] the parameter $R_{min}K_{max}$ can be controlled, the required values lie between 7.5 and 9. When making a series of calculations with the aim of comparing the results, the same value of $R_{min}K_{max}$ should be used in all calculations. In this work the value $R_{min}K_{max} = 7$ is used, unless otherwise indicated. Finding the best $R_{mt}K_{max}$ is important, especially when doing big calculations that require a lot of time. The basis should be large enough to have accuracy, but not too large and waste time. To test the basis, it is a good idea to calculate total energy and a sensitive quantity (such as the electric field gradient) as a function of the size of the k-mesh used and $R_{mt}K_{max}$. The k-mesh is the number of points used to divide the reciprocal space. When these quantities are converging it gives a good idea of the optimal value for each of these parameters.

LAPW and local orbitals

Sometimes the character of a state is a mixture of core and valence, such a state is called a semicore state. It happens sometimes with states with the same quantum number l but different n . In those cases the optimal solution is not the sphere or interstitial region, and the calculation can be improved by adding more basis functions to the LAPW basis set, called local orbitals. A local orbital is defined as

$$\Phi_{\alpha,LO}^{lm}(\mathbf{r}) = \begin{cases} 0 & \mathbf{r} \notin \mathbf{S}_{\alpha} \\ \left(A_{l,m}^{\alpha,LO} u_l^{\alpha}(r', E_{1,l}^{\alpha}) + B_{lm}^{\alpha,LO} \dot{u}_l^{\alpha}(r', E_{1,l}^{\alpha}) + C_{l,m} u_l^{\alpha}(r', E_{2,l}^{\alpha}) \right) Y_m^l(\hat{r}') & \mathbf{r} \in \mathbf{S}_{\alpha} \end{cases}$$

A local orbital is zero in the interstitial region and is specific to the muffin tin sphere of one atom, hence its name local orbital. The three coefficients are determined by requiring that the local orbital has zero value and slope at the sphere boundary, and is normalized. Increasing the basis set with local orbitals is often synonym of much better accuracy with only a little more computational time, so the code Wien2k uses them by default.

APW+lo method[34]

The APW+lo basis set has not the same problem of the APW. This was achieved at the cost of a larger basis set. APW+lo has the advantage of a basis of the same size as in APW. As the name indicates, this method uses the two kinds of functions, APWs and local orbitals. The local orbitals however are not of the same type of local orbitals used with LAPW. They are defined as

$$\phi_{\mathbf{K}}^{\mathbf{k}} = \begin{cases} \frac{1}{\sqrt{V}} e^{i(\mathbf{k}+\mathbf{K})\mathbf{r}} & \mathbf{r} \in \mathbf{I} \\ \sum_{l,m} A_{l,m}^{\alpha,\mathbf{k}+\mathbf{K}} u_l^{\alpha}(r' E_{1,l}^{\alpha}) Y_m^l(\hat{r}') & \mathbf{r} \in \mathbf{S}_{\alpha} \end{cases}$$

Mixed basis sets (LAPW/APW+lo)

Some particular states are harder (need a larger number of basis functions to be described correctly) for LAPW than for APW+lo, and this results in a larger K_{max} needed for LAPW. It is possible to treat those states with APW+lo and keep using LAPW for other states. The advantage of this choice is keeping the $R_{min} K_{max}$ low for accurate results. This mixed basis set is the recommended basis choice in WIEN2k.

APW+lo with local orbitals (APW+lo+LO)

The type of local orbitals used in APW(lo) are different from the local orbitals (LO) used in LAPW. Using APW+lo, the same problem of treating semi-core states appears as in LAPW (3.1.6). By adding the same local orbitals as in LAPW this problem is solved.

3.2 Electric field gradient in LAPW

One is most interested in the principal component of the electric field gradient, V_{zz} or V_{20} (spherical). The principal component can be obtained from the charge density by

$$V_{zz} = \int \rho(r) \frac{2P_2(\cos\vartheta)}{r^3} dr \quad (3.29)$$

$P_2(\cos\vartheta)$ is the Legendre Polynomial

$$P_n(x) = \frac{1}{2^n n!} \frac{d^n}{dx^n} [(x^2 - 1)^n]. \quad (3.30)$$

The V_{xx} , V_{yy} (and η) are obtained in an analogous way.

Chapter 4

Results and discussion

4.1 Method

The code used with DFT as the basis is Wien2k[7, 35]. It is a computational tool that consists in a set of routines, (individual FORTRAN programs linked by C shell-scripts) developed by P. Blaha, K. Schwarz, G. Madsen, D. Kvasnicka and J. Luitz from the Inst. f. Materials Chemistry, TU Vienna. It can calculate total energy, forces, and other important properties to the understanding of materials such as hyperfine parameters (electric field gradient, magnetic hyperfine field, and isomer shifts), density of states, X-ray spectra, phonons or optical properties.

The required input are structural parameters of a unit cell. This input is used to generate a starting electronic density. Each iteration consists on using an electronic density to calculate a Kohn-Sham potential, that in turn calculates a new electronic density. Then convergence may be obtained, when the difference between results of successive cycles is smaller than a given value, defined by the user. It is an *ab initio* or first-principles method, which means that the given structural parameters can be optimized, by minimization of the total energy, or forces at the atomic sites. It is possible to make a structural optimization based on the variation of the volume or by variation of atomic internal parameters. In the case of mixed compounds, such as $\text{La}_{1-x}\text{Ca}_x\text{MnO}_3$, one has to include occupancy probabilities and use layer unit cells to account for the atoms stoichiometry(x). This can be very lengthy for non rational values of x. The method was applied and results were obtained, with some of the perovskite structure family of manganese based oxides described in section 2.1.3.

After learning to install and adapt the operating system¹ in a computer,

¹in this particular case openSuSE 10.2, other Unix based systems are also compatible

compiling the programs, repetition of the process on another computer, and using also a cluster of another two computers, the computational power to perform a good number of simulations was available. An important point to get acquainted with these methods is to study simple situations, and analyzing the influence of input data on the final results.

4.2 CaMnO₃

CaMnO₃ is one of the simplest manganites, that is practically undistorted at low temperatures, since it has only Mn⁴⁺. I started with the simple high symmetry cubic perovskite structure. Evidently the EFG at the Ca site is zero, as it is at the Mn site. In the bulk stable state CaMnO₃ is a G-type antiferromagnetic semiconductor. The ionic picture Ca²⁺Mn⁴⁺O₃²⁻, with spherical Mn d³ configuration makes the face centered cubic phase stable over distortions observed, for example, in LaMnO₃, with Jahn-Teller Mn³⁺ ions.

A test was then performed a unit cell with $a = 3.72666$, $b = 37020$ and $c = 3.73303\text{\AA}$, values obtained from x-ray measurements[11]. These values were calculated from the orthorhombic distorted cell with 4 formula units (measured values of $a = 5.2703\text{\AA}$, $b = 5.2753\text{\AA}$ $c/\sqrt{2} = 5.2793\text{\AA}$) to a smaller primitive cell by $a_P = a/\sqrt{2}$, $b_P = b/\sqrt{2}$ and $c_P = c/2$.

I performed a series of tests to check the sensitivity of the calculation to structure changes and errors in the input values. The value of η seems to vary significantly with a small change (0.001 Å) at the edges of the unit cell. Everyone of these tests used as input parameters: a 64 k-point mesh in the irreducible Brillouin zone and a convergence parameter $RK_{max} = 7$. The calculation considered spin-polarization. The results obtained by varying a and c are presented in the tables 4.1 and 4.2.

Table 4.1: Asymmetry parameter η

$a/c(\text{\AA})$	3.73103	3.73203	3.73303	3.73403	3.73503
3.72466	0.23430	0.43053	0.62062	0.81669	0.95993
3.72566	0.25964	0.56880	0.73199	0.93036	0.91612
3.72666	0.33027	0.62004	0.82767	0.90404	0.76382
3.72766	0.41759	0.76132	0.94455	0.73688	0.61320
3.72866	0.56059	0.92422	0.65360	0.49625	0.38327

A contour plot of the values of η is also presented in the figure 4.2.

It is seen that a change of 10^{-3}\AA on a unit cell edge already translates into a substantial variation of EFG and η . The EFG obtained with PAC

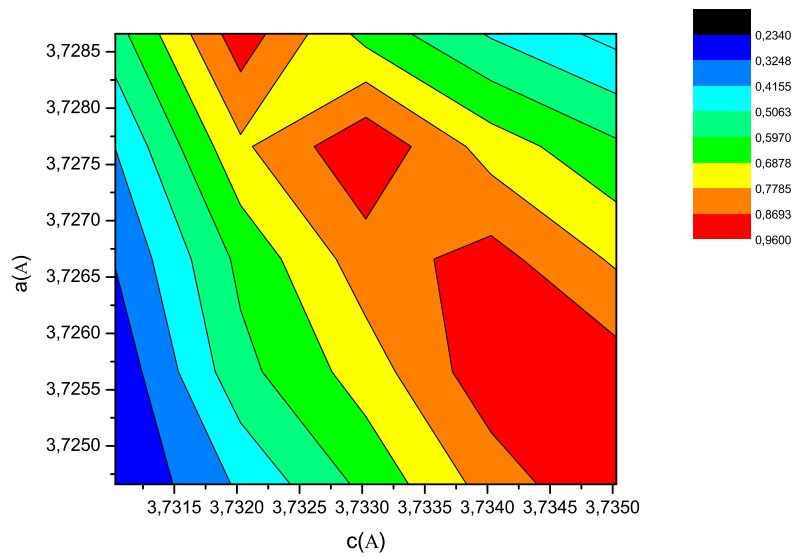


Figure 4.1: Values of the asymmetry parameter calculated by varying a or c edges in a perovskite unit cell without distortions, for the case of CaMnO_3

Table 4.2: $V_{zz}(V/\text{\AA}^2)$

$a/c(\text{\AA})$	3.73103	3.73203	3.73303	3.73403	3.73503
3.72466	-0.16070	-0.11490	-0.10710	-0.13370	-0.14280
3.72566	-0.08780	-0.09680	-0.12460	-0.11670	0.13070
3.72666	-0.07140	-0.08010	-0.08130	0.10400	0.12210
3.72766	-0.05640	-0.06510	0.07650	0.09620	0.11440
3.72866	-0.03650	0.04740	0.06670	0.08660	0.10500

[11] is $V_{zz} = 58.2V/\text{\AA}^2$ and $\eta = 0.66$. The obtained deviation with experiment can be explained qualitatively considering the distortions not taken in account by the cubic input structure. The obtained V_{zz} has a qualitative expected behavior, since the deviation from cubic symmetry corresponds to an increase of the absolute value. However, comparing with experimental results obtained with PAC[40] ($V_{zz} = 58.2V/\text{\AA}^2$, $\eta = 0.66$), the obtained values of V_{zz} are too small. Even though the calculated EFG sensibility is high, the experimental value is on another scale. Probably something is not being taken into account in the theoretical calculations. Maybe the refinement needed to the structural data, taking the octahedral distortions into account, will increase the EFG. The values of η have a great variation with the lattice parameters. For some of the cases calculated, η is very close to the experimental value.

4.3 LaMnO₃

4.3.1 Previous work

Although the properties of this manganite are quite difficult to simulate because of its complexity, there is some literature available on the subject. The LSDA calculations often fail to predict the insulating behavior of LaMnO₃. To correct this deficiency of the LSDA to give the right insulating properties of the perovskites, LSDA+U theory can be applied, where U is an intrasite Coulomb repulsion added to the calculations. Hu et al.[46] reported that to get the correct experimental ground state for LaMnO₃, it is necessary to take Jahn-Teller distortion, electron-electron correlations, and antiferromagnetic ordering simultaneously into consideration. Some of the features lacking in most of the theoretical studies on LaMnO₃ originate also from the fact that they have often resulted from use of the atomic-sphere approximation, which means that the calculations have not included the non spherical part of the potential. Also calculations sometimes use a minimal basis set, and

the cubic perovskite structure is frequently assumed, neglecting significant structural distortions, probably because the orthorhombic structure greatly increases the computational time. While for the case of CaMnO_3 the ground state (where theory can be used) has almost no distortions, LaMnO_3 is more complicated in this respect and the orthorhombic structure must be used to reproduce even basic features. Spin-orbit coupling is another interaction which may be of significance for calculations in this material, and has not been included in earlier studies. Instead of using the uniform electron gas limit for exchange and correlations corresponding to the LSDA, the outcome is also improved by including inhomogeneity effects through the Perdew and Burke parametrization of the generalized gradient approximation (GGA) [38]. The first principles pseudo potential method is also used [38] to perform structural optimization, based on the approximations LDA, GGA, and LDA+U, and it can successfully reproduce Jahn-Teller distortions with all three methods, although the magnitude of the distortions obtained isn't quite as large as the experimental value. The same analysis is performed with a hypothetical ferromagnetic state and the distortions almost vanish, with lower total energy predicted by ferromagnetic ordering. This is a result incoherent with experimental observation, since in reality for the ground-state of LaMnO_3 antiferromagnetic ordering is observed. Fuks et al. [45] obtained the density of states for cubic LaMnO_3 and SrMnO_3 , to serve as a first step study of the strontium doped lanthanum manganite. The individual compounds have a cubic structure at relatively high temperatures, and this study serves to give an understanding of each structure.

4.3.2 Results

The DOS graphics were obtained, also with Wien2k. For this work, the same calculation was successfully reproduced, and the obtained density of states graphics are reproduced in the next pages. Fuks et. al also obtained electron density plots of SrMnO_3 with the planes of Sr-O and Mn-O bonds, which agree with experimental results, showing that the Sr-O bonds are ionic but the Mn-O bonds are partially covalent. For the LaMnO_3 obtained density of states, it is interesting to see that there is a gap for one spin but not for the other.

In the calculations with LaMnO_3 for this work, spin orbit interaction was not used, the exchange-correlation approximation used was GGA and with spin-polarization, and the structure used takes Jahn-Teller distortions into account. Using a structure of this type the asymmetry parameter obtained ($\eta = 0.84$) agrees with experimental values obtained with PAC [11], NMR [42, 43] and with other FLAPW calculations [47] ($\eta = 0.9$). The obtained

value of V_{zz} , although not with a precise agreement, is at least of the same order, $V_z = 135V/\text{\AA}^2$ which compares reasonably with $V_{zz} = 71.7V/(\text{\AA})$ obtained at $10.9K$ for the stoichiometric sample with PAC[41]. The theoretical value is two times the experimental value which is not bad compared with another result from literature obtained with first principles FLAPW [47], for which the obtained EFG is two $V_{zz} = 35.79$ and $V_{zz} = -15.87V/\text{\AA}^2$, for the ferromagnetic and antiferromagnetic phases respectively.

From the analysis of the density of states of LaMnO_3 one can see that it is close to a 100% spin polarized conduction band, if the Fermi energy is reduced. This can be achieved by reducing the number of electrons in the system, doping with a divalent metal to increase the $\text{Mn}^{4+}/\text{Mn}^{3+}$ ratio.

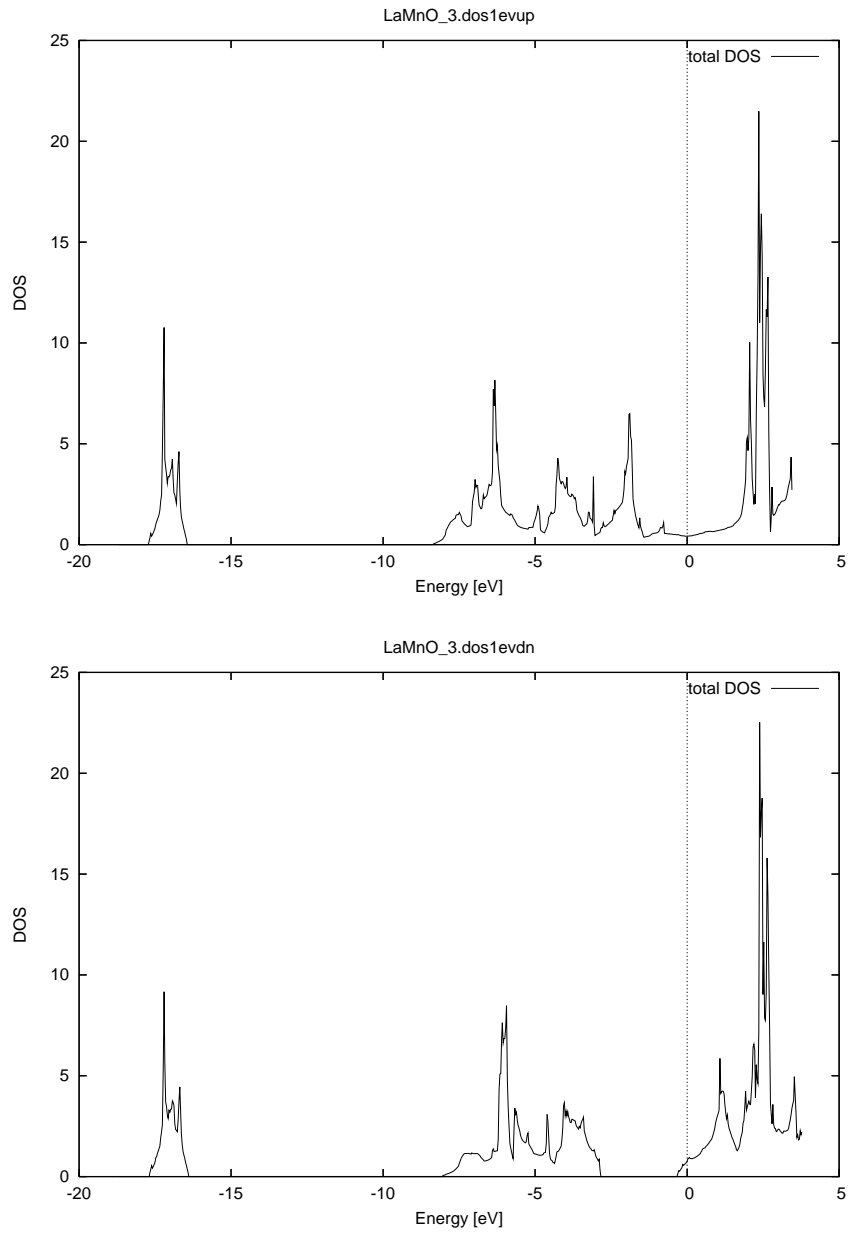


Figure 4.2: Density of states corresponding to the up and down spin states, for the cubic structure of LaMnO₃. The zero value in energy corresponds to the Fermi energy.

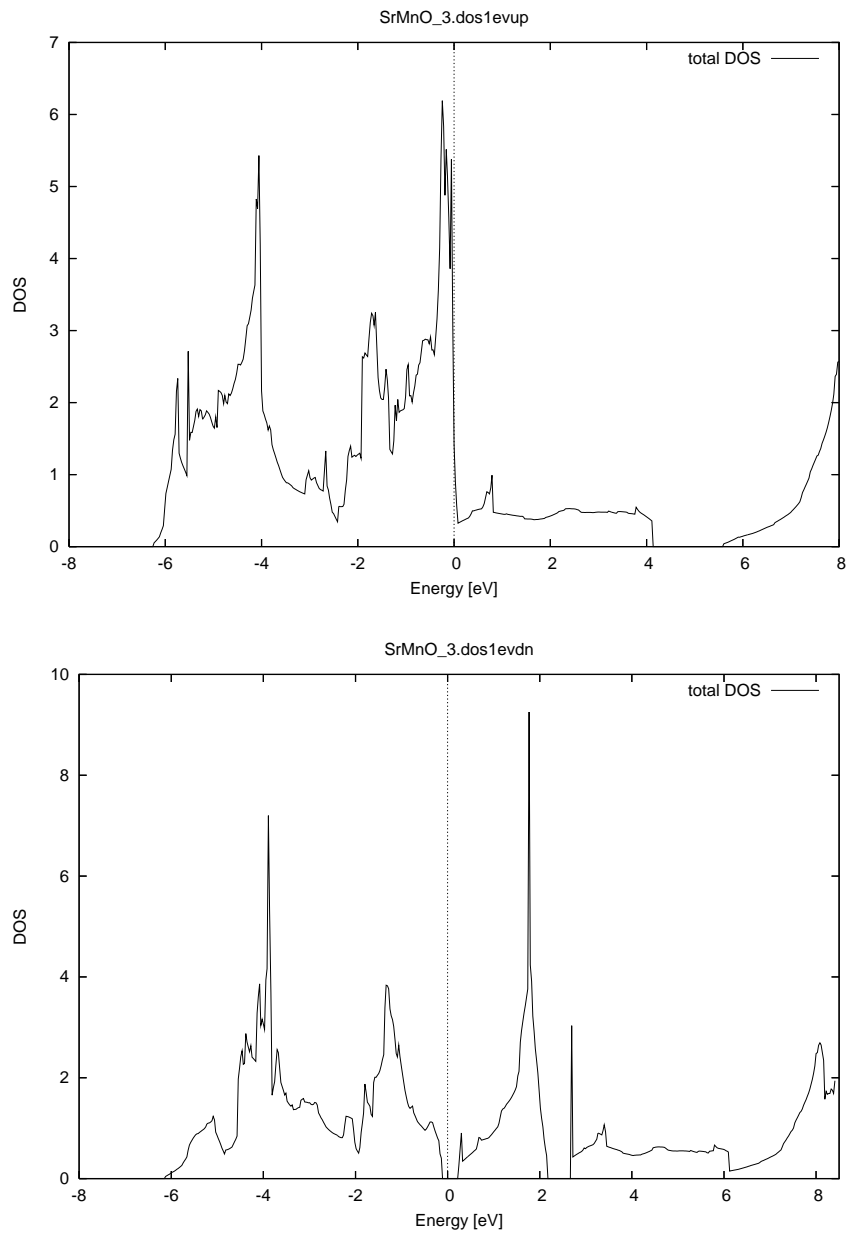


Figure 4.3: Density of states corresponding to the up and down spin states, for the cubic structure of SrMnO_3 . The zero value in energy corresponds to the Fermi energy.

Chapter 5

Conclusion

The band structure calculations resulted in some interesting results. Some are in disagreement with experimental results, and it will be interesting to see the effect of one or other approximation and input values for the improvement of these results in the future. The results show that the electric field gradient is highly sensible to the use of different approximations, or structural and magnetic variations. Due to this high sensitivity it is a good quantity to test experimentally aspects of different theoretical approaches of materials. The electronic density of states for the LaMnO_3 hypothetical cubic phase agrees with published results, however the electric field gradient can be improved with the use of other effects in the calculation. The values of V_{zz} for CaMnO_3 are very far from experimental values and an explanation cannot be given at this point, it will be interesting to see in the future why this is happening. Probably the distortions, not taken into account, have a huge effect in the electric field gradient, which explains the small values obtained.

Concluding, Wien2k is an well established method that can give good results for the electric field gradient, and many other properties of interest. It may help in experimental physics, even if the results are only of qualitative value, to separate good experiences from those not worth doing. In theory, the accuracy of the method is well known as one of the best, and predictions about all kinds of properties of materials are always useful.

List of Tables

1.1	Low temperature EFG parameters for some samples of the series $\text{Pr}_{1-x}\text{Ca}_x\text{MnO}_3$ and for the compositions $x=0.05, 0.14$ and 0.95 , and for three different low temperatures [11].	19
2.1	Shannon ionic radii of common elements present in perovskite structure oxides(\AA)[15]	22
4.1	Asymmetry parameter η	43
4.2	$V_{zz}(V/\text{\AA}^2)$	45

List of Figures

1.1	Decay of isotope ^{111}In and ^{111m}Cd cascade. Intermediate PAC probe state, with energy $E=254.4$ keV, half life $t_{1/2} = 84.\text{ns}$ and angular momentum $I=5/2$	13
1.2	ISOLDE Hall	14
1.3	Left: System of 4 detectors used for PAC spectroscopy. Right: System of 6 detectors.	15
1.4	PAC spectrum for ^{111}Cd in cadmium metal. Coincidence count rates $N(\theta,t)$ for $\theta = 90^\circ$ and $\theta = 180^\circ$	16
1.5	$R(t)$	17
1.6	Experimental functions $R(t)$ (left) and corresponding Fourier spectra(right) for CaMnO_3 at 80 K(top) and 10K(bottom). Fits to the experimental spectra are the continuous lines over $R(t)$ and the Fourier transform. Taken from [11].	18
1.7	Experimental functions $R(t)$ (left) and corresponding Fourier spectra(right) for PrMnO_3 at 77 K(top) and 10K(bottom). Fits to the experimental spectra are the continuous lines over $R(t)$ and the Fourier transform. Taken from [11].	18
2.1	Ideal structure ABO_3 , A the atoms at the corners, O the face centered atoms and B at the center.	21
2.2	Field splitting of the degenerate atomic 3d levels into lower t_{2g} and higher e_g levels. The particular Jahn-Teller distortion lifts each degeneracy as shown, for the case of Mn^{3+} [16].	23
2.3	The GdFeO_3 -type crystal structure of LaMnO_3 , an orthorhombically distorted perovskite-type structure.	24
2.4	Sketch of the double exchange mechanism, which involves two Mn ions and one O ion.	25
2.5	Some possible modes for the B-site cations in the perovskite structure(solid and open circles represent two antiferromagnetic sublattices)[12]	26

2.6	Example of the complex phase diagrams obtained by varying composition and temperature of manganites, in this case with $\text{La}_{1-x}\text{Ca}_x\text{MnO}_3$ [21]	27
2.7	Example of the complex phase diagrams obtained by varying composition and temperature of manganites, in this case with $\text{Pr}_{1-x}\text{Ca}_x\text{MnO}_3$ [22]	27
3.1	Flow Chart for the n^{th} iteration in the selfconsistent procedure to solve the Kohn-Sham equations[27].	34
4.1	Values of the asymmetry parameter calculated by varying a or c edges in a perovskite unit cell without distortions, for the case of CaMnO_3	44
4.2	Density of states corresponding to the up and down spin states, for the cubic structure of LaMnO_3 . The zero value in energy corresponds to the Fermi energy.	48
4.3	Density of states corresponding to the up and down spin states, for the cubic structure of SrMnO_3 . The zero value in energy corresponds to the Fermi energy.	49

Bibliography

- [1] S. Jin , T. H. Tiefel , M. McCormack , R. A. Fastnacht , R. Ramesh and L. H. Chen, "Thousandfold Change in Resistivity in Magnetoresistive La-Ca-Mn-O Films", *Science*, Vol. 264. no. 5157, pp. 413 - 415 (1994).
- [2] G. H. Jonker, and J. H. van Santen, "Ferromagnetic compounds of manganese with perovskite structure", *Physica*, 16, 337 (1950).
- [3] J. H. van Santen and G. H. Jonker, "Electrical Conductivity of ferromagnetic compounds of manganese with perovskite structure", *Physica*, 16, 599 (1950).
- [4] G. H. Jonker and J. H. van Santen, "Magnetic compounds with perovskite structure III. ferromagnetic compounds of cobalt", *Physica*, 19, 120 (1953).
- [5] C. Zener, "Interaction between the d-Shells in the Transition Metals. II. Ferromagnetic Compounds of Manganese with Perovskite Structure", *Physical Review*, 16, pp.337-349(1950).
- [6] P. Anderson and H. Hasegawa, "Considerations on Double Exchange", *Physical Review*, vol.100, no. 2, pp.675-681, (1955).
- [7] P. Blaha, K. Schwarz, G. K. Madsen, D. Kvasnicka and J. Luitz, *WIEN2k, An Augmented Plane Wave Plus Local Orbitals Program for Calculating Crystal Properties*. ISBN 3-9501031-1-2, Vienna University of Technology, Austria, 2001.
- [8] G. Schatz and A. Weidinger, "Nuclear condensed matter physics", John Wiley and Sons, England(1996).
- [9] R. Eisberg, "Quantum physics of atoms, molecules, solids, nuclei and particles", John Wiley and Sons, USA(1985).
- [10] P. Blaha, K. Schwarz, W. Faber, and J. Luitz, *Hyperfine Interact.*, "Calculations of electric field gradients in solids: How theory can complement experiment", *Hyperfine interac.* 126, 389(2000).

- [11] A. M. L. Lopes, "Local probe studies on lattice distortions and electronic correlations in manganites", Phd thesis, Universidade de Aveiro(2006).
- [12] J. M. D. Coey, M. Viret and S. V. Molnar, "Mixed-valence manganites", *Advances In Physics* (1999).
- [13] Fabricius, G. and García, A. López, "First-principles study of the orthorhombic $CdTiO_3$ perovskite", *Phys. Rev. B* 66, 233106 (2002).
- [14] V. M. Goldschmidt, *Geochemistry*, Oxford University Press(1958).
- [15] R. D. Shannon and C. T. Prewitt, "Effective ionic radii in oxides and fluorides", *Acta crystallogr. B*, (1969).
- [16] Y. Tokura and Y. Tomioka, "Colossal magnetoresistive manganites", *Journal of Magnetism and Magnetic Materials*(1999).
- [17] Ken-ichi Chahara, T. Ohno, M. Kasai and Y. Kozono, "Magnetoresistance in magnetic manganese oxide with intrinsic antiferromagnetic spin structure", *Applied Physics Letters*, Volume 63, Issue 14, pp. 1990-1992 (1993).
- [18] R. von Helmolt, J. Wecker, B. Holzäpfel, L. Schultz and K. Samwer, "Giant negative magnetoresistance in perovskitelike $La_{2/3}Ba_{1/3}MnO_x$ ferromagnetic films", *Phys. Rev. Lett.* 71, 2331 - 2333 (1993).
- [19] A. J. Millis, P. B. Littlewood and B. I. Shraiman, "Double exchange alone does not explain the resistivity of $La_{1-x}Sr_xMnO_3$ ", *Physical Review Letters* 74, no. 25, pp.5144-5147 (1995).
- [20] D. D. Sarma, D. Topwal, U. Manju, S. R. Krishnakumar, M. Bertolo, S. La Rosa, G. Cautero, T. Y. Koo, P. A. Sharma, S.-W. Cheong and A. Fujimori, "Direct Observation of Large Electronic Domains with Memory Effect in Doped Manganites", *Physical Review Letters*, vol.93,no. 9,pp. 097202 (2004).
- [21] P. Schiffer, A. P. Ramirez, W. Bao and S-W. Cheong, "Low Temperature Magnetoresistance and the Magnetic Phase Diagram of $La_{1-x}Ca_xMnO_3$ ", *Phys. Rev. Lett.* 75, 3336 - 3339 (1995).
- [22] C. Martin, A. Maignan, M. Hervieu and B. Raveau, "Magnetic phase diagrams of $L_{1-x}A_xMnO_3$ manganites (L=Pr,Sm;A=Ca,Sr)", *Physical Review B*, vol. 60, no. 17, pp. 12191-12199, November (1999).

- [23] G. Pari, S. Mathi Jaya, G. Subramoniam and R. Asokamani, “Density functional description of the electronic structure of LAMO_3 (M=Sc,V,Cr,Mn,Fe,Co,Ni)”, Phys. Rev. B 51, 16 575 (1995).
- [24] P. Hohenberg and W. Kohn, “Inhomogeneous electron gas”, Phys. Rev. 136 B864 (1964).
- [25] W. Kohn and L. J. Sham, “Self-consistent equations including exchange and correlation effects”, Phys. Rev. 140 A1133 (1965).
- [26] P.A.M. Dirac, ”Note on exchange phenomena in the Thomas atom”, Proc. R. Soc. Camb. Phil. Soc. 26, 376-395 (1930).
- [27] S. Cottenier, “Density Functional Theory and the family of (L)APW-methods: a step-by-step introduction (Instituut voor Kern-en Stralingsfysica, K.U.Leuven, Belgium)”, ISBN (2002).
- [28] Perdew, John P. and Burke, Kieron and Ernzerhof, Matthias, “Generalized Gradient Approximation Made Simple”, Phys. Rev. Lett. 77, 3865 - 3868 (1996).
- [29] Perdew, John P. and Kurth, Stefan and Zupan, Aleš and Blaha, Peter, ”Accurate Density Functional with Correct Formal Properties: A Step Beyond the Generalized Gradient Approximation”, Phys. Rev. Lett. 82 12 2544–2547 (1999).
- [30] Tao, Jianmin and Perdew, John P. and Staroverov, Viktor N. and Scuseria, Gustavo E., ”Climbing the Density Functional Ladder: Nonempirical Meta-Generalized Gradient Approximation Designed for Molecules and Solids”, Phys. Rev. Lett. 91, 14 (2003).
- [31] J. C. Philips, ”Energy-Band Interpolation Scheme Based on a Pseudopotential” Phys. Rev., 112 (1958).
- [32] J. C. Slater, ”Wave Functions in a Periodic Potential”, Phys. Rev. 51, 846 - 851 (1937).
- [33] D. Singh, ”Plane waves, pseudopotentials and the LAPW method”, Kluwer Academic (1994)
- [34] E. Sjstedt, L. Nordstorm and DJ Singh, Solid State Commun. 114 (2000).
- [35] <http://www.wien2k.at>

- [36] E. O. Wollan and W. C. Koehler, “Neutron diffraction study of magnetic properties of the series of perovskite-type compounds $\text{La}_{1-x}\text{Ca}_x\text{MnO}_3$ ”, Phys. Rev. 100, 545 (1955).
- [37] C. N. R. Rao and B. Raveau, “Colossal Magnetoresistance, Charge Ordering, and Related Properties of Manganese Oxides”, World Scientific, Singapore (1998).
- [38] H. Sawada, Y. Morikawa, K. Terakura and N. Hamada, *Jahn Teller distortion and magnetic structures in LaMnO_3* , PhysRevB.56.12154
- [39] J. P. Perdew, K. Burke and M. Ernzerhof, “Generalized Gradient Approximation Made Simple”, Phys. Rev. Lett. 77, 3865 (1996).
- [40] A. M. L. Lopes, J. P. Araújo, E. Rita, J.G. Correia, V. S. Amaral, Y. Tomioka, Y. Tokura, and R. Suryanarayanan, ”Perturbed angular correlation study of $\text{Pr}_{1-x}\text{Ca}_x\text{MnO}_3$ ”, Journal of Magnetism and Magnetic Materials, 272, E1667-E1668(2004).
- [41] A. M. L. Lopes, J. P. Arajo, E. Rita, J. G. Correia, M. S. Reis, V. S. Amaral, R. Suryanarayanan, and ISOLDE Collaboration, “Local probe studies on $\text{LaMnO}_3+\Delta$ using the Perturbed Angular Correlation Technique”, Journal of Magnetism and Magnetic Materials, 272, E1671-E1673(2004).
- [42] K. Kumagai et al., “Microscopically homogeneous magnetic structure of $\text{La}_{12}\text{xSr}_x\text{MnO}_3$ beyond the range of $0 < x < 0.1$ observed by La NMR”, Phys. Rev. B 59, 97 (1999).
- [43] G. Allodi, M. C. Guidi, R. De Renzi, A. Caneiro, and L. Pinsard, “Ultra-slow Polaron Dynamics in Low-Doped Manganites from ^{139}La NMR-NQR and Muon Spin Rotation”, Phys. Rev. Lett. 87, 127206 (2001).
- [44] P. Ravindran, A. Kjekshus, H. Fjellvg, and O. Eriksson, “Ground-state and excited-state properties of LaMnO_3 from full-potential calculations”, Phys. Rev. B 65, 064445 (2002).
- [45] D. Fuks, S. Dorfman, J. Felsteiner, L. Bakaleinikov, A. Gordon and E. A. Kotomin, “Ab initio calculations of atomic and electronic structure of LaMnO_3 and SrMnO_3 ” Solid State Ionics 173 (1-4 SPEC. ISS.), pp. 107-111(2004).
- [46] W. Y. Hu, M. C. Qian, Q. Q. Zheng, H. Q. Lin, and H. K. Wong, “Jahn-Teller effect and many-body correlation effect in LaMnO_3 ” Phys. Rev. B 61, 1223 (2000).

- [47] P. Ravindran, A. Kjekshus, H. Fjellvag, A. Delin and O Eriksson, "Ground-state and excited-state properties of LaMnO_3 from full-potential calculations", Phys. Rev. N, 064445 (2002).